

Enhanced moments of Eu in single crystals of the metallic helical antiferromagnet $\text{EuCo}_{2-y}\text{As}_2$

N. S. Sangeetha,¹ V. K. Anand,^{1,*} Eduardo Cuervo-Reyes,^{2,3} V. Smetana,⁴ A.-V. Mudring,⁴ and D. C. Johnston^{1,5}

¹*Ames Laboratory, Iowa State University, Ames, Iowa 50011, USA*

²*Swiss Federal Laboratories for Materials Science and Technology (Empa),
Überlandstrasse 129, CH-8600 Dübendorf, Switzerland*

³*Swiss Federal Institute of Technology (ETH), Vladimir-Prelog-Weg 1, CH-8093 Zürich, Switzerland[†]*

⁴*Department of Materials and Environmental Chemistry,*

Stockholm University, Svante Arrhenius väg 16 C, 106 91 Stockholm, Sweden

⁵*Department of Physics and Astronomy, Iowa State University, Ames, Iowa 50011*

(Dated: July 5, 2021)

The compound $\text{EuCo}_{2-y}\text{As}_2$ with the tetragonal ThCr_2Si_2 structure is known to contain Eu^{+2} ions with spin $S = 7/2$ that order below a temperature $T_N \approx 47$ K into an antiferromagnetic (AFM) proper helical structure with the ordered moments aligned in the tetragonal ab plane, perpendicular to the helix axis along the c axis, with no contribution from the Co atoms. Here we carry out a detailed investigation of the properties of single crystals. We consistently find about 5% vacancies on the Co site from energy-dispersive x-ray analysis and x-ray diffraction refinements. Enhanced ordered and effective moments of the Eu spins are found in most of our crystals. Electronic structure calculations indicate that the enhanced moments arise from polarization of the d bands, as occurs in ferromagnetic Gd metal. Electrical resistivity measurements indicate metallic behavior. The low-field in-plane magnetic susceptibilities $\chi_{ab}(T < T_N)$ for several crystals are reported that are fitted well by unified molecular field theory (MFT), and the Eu–Eu exchange interactions J_{ij} are extracted from the fits. High-field magnetization M data for magnetic fields $H \parallel ab$ reveal what appears to be a first-order spin-flop transition followed at higher field by a second-order metamagnetic transition of unknown origin, and then by another second-order transition to the paramagnetic (PM) state. For $H \parallel c$, the magnetization shows only a second-order transition from the canted AFM to the PM state, as expected. The critical fields for the AFM to PM transition are in approximate agreement with the predictions of MFT. Heat capacity C_p measurements in zero and high H are reported. Phase diagrams for $H \parallel c$ and $H \parallel ab$ versus T are constructed from the high-field $M(H, T)$ and $C_p(H, T)$ measurements. The magnetic part $C_{\text{mag}}(T, H = 0)$ of $C_p(T, H = 0)$ is extracted and is fitted rather well below T_N by MFT, although dynamic short-range AFM order is apparent in $C_{\text{mag}}(T)$ up to about 70 K, where the molar entropy attains its high- T limit of $R \ln 8$.

I. INTRODUCTION

Many studies of iron-based layered pnictides and chalcogenides have appeared due to their unique lattice, electronic, magnetic and superconducting properties [1–9]. An important family of these materials consists of doped and undoped compounds $A\text{Fe}_2\text{As}_2$ ($A = \text{Ca}, \text{Sr}, \text{Ba}, \text{Eu}$) with the body-centered tetragonal ThCr_2Si_2 structure with space group $I4/mmm$ (122-type compounds). Searches for novel physical properties in various 122-type compounds with other transition metals replacing Fe have been carried out, such as for Mn [10–19] and Cr [20–27].

Here we are concerned with $A\text{Co}_2\text{As}_2$ and $A\text{Co}_2\text{P}_2$ compounds (Co122 systems) with the ThCr_2Si_2 structure that have also attracted much interest due to their rich magnetic behaviors, where the electronic states of the CoAs and CoP layers are sensitive to the crystal struc-

ture. By forming As–As and P–P bonds along the c axis, their crystal structures can collapse along this axis, resulting in the so-called collapsed-tetragonal (cT) structure which is to be distinguished from the uncollapsed-tetragonal (ucT) structure. In contrast to the Fe122 compounds that exhibit a magnetic to nonmagnetic transition under pressure coincident with a ucT to cT transition, the Co-based compounds behave in the opposite manner, with the ambient-pressure ucT compounds being paramagnetic and the cT compounds exhibiting magnetic ordering [28]. For example, $\text{CaCo}_{2-y}\text{As}_2$ has a cT structure at ambient pressure and manifests itinerant A-type antiferromagnetic (AFM) ordering with the ordered moments aligned along the c axis [29, 30], whereas the 122-type SrCo_2As_2 and BaCo_2As_2 compounds have ucT structures with no long-range magnetic ordering [31, 32]. Inelastic neutron scattering and NMR studies on SrCo_2As_2 have revealed strong stripe-type AFM correlations at high energies whereas NMR measurements reveal strong FM correlations at low energies [33, 34]. On the other hand, the system $\text{SrCo}_2(\text{Ge}_{1-x}\text{P}_x)_2$ develops weak itinerant ferromagnetism during the course of the dimer breaking, and a quantum critical point (QCP) is observed at the onset of the FM phase, although both SrCo_2P_2 (ucT) and SrCo_2Ge_2 (cT) are paramagnetic (PM) [35].

*Present address: Helmholtz-Zentrum Berlin für Materialien und Energie GmbH, Hahn-Meitner Platz 1, D-14109 Berlin, Germany

[†]Present address: ABB Corporate Research Ltd., CH-5405, Baden-Daettwil, Switzerland

From first-principles calculations, it was shown that the degree of As-As covalent bonding in CaFe_2As_2 and the magnitude of the spin on the Fe atoms are inversely related [36, 37]. Similarly, the magnetic properties of the cobalt pnictides were correlated with changes in the formal Co charge as determined by the estimated degree of P-P covalent bonding along the c axis [38].

EuCo_2P_2 is an interesting ucT compound in the Co122 family. It shows AFM ordering of the Eu^{2+} spins $S = 7/2$ below $T_N = 66$ K [39]. Neutron diffraction studies demonstrated that the AFM structure is a planar helix with the Eu ordered moments aligned in the ab plane of the tetragonal structure, and with the helix axis being the c axis [40]. This compound shows a pressure-induced first-order ucT to cT transition at ≈ 3 GPa [41] associated with the valence change of Eu from Eu^{2+} to nonmagnetic Eu^{3+} together with the emergence of itinerant $3d$ magnetism in the Co sublattice, which orders AFM at $T_N^{\text{Co}} = 260$ K [42]. We showed that EuCo_2P_2 is a textbook example of a noncollinear helical antiferromagnet for which the thermodynamic properties in the antiferromagnetic state are well described by our unified molecular field theory (MFT) [43].

EuCo_2As_2 also has the ucT 122-type structure and hence is isostructural and isoelectronic to EuCo_2P_2 [44, 45]. It exhibits AFM ordering of the Eu^{+2} spins- $7/2$ at $T_N = 47$ K [46, 47]. Neutron diffraction measurements showed that the AFM structure is the same coplanar helical structure as in EuCo_2P_2 , with no participation by Co moments [44]. Here the reported helix propagation vector is $\mathbf{k} = (0, 0, 0.79)(2\pi/c)$ [44], very similar to that of EuCo_2P_2 which is $\mathbf{k} = (0, 0, 0.85)(2\pi/c)$ [40]. The c/a ratios of EuCo_2P_2 (3.01) and EuCo_2As_2 (2.93) are also similar and both indicate a ucT structure. High-pressure measurements on EuCo_2As_2 showed a continuous tetragonal to collapsed tetragonal crossover at a pressure $p \approx 5$ GPa [48] and a change in the associated valence state of Eu, achieving the average oxidation state of $\text{Eu}^{+2.25}$ at 12.6 GPa. As a result, ferromagnetic (FM) ordering arises from both Eu and Co moments with a Curie temperature $T_C = 125$ K, which is confirmed by x-ray magnetic circular dichroism measurements and electronic structure calculations.

One reason for carrying out the present detailed study of $\text{EuCo}_{2-y}\text{As}_2$ is that the reported effective magnetic moment in the paramagnetic (PM) state $\mu_{\text{eff}} \approx 8.22 \mu_B/\text{Eu}$ is significantly larger than the value of $\mu_{\text{eff}} = 7.94 \mu_B$ expected for Eu^{2+} [45] (see also Table I below). Normally, the effective and ordered moments of Eu^{+2} and Gd^{+3} are rather robust due to the spin-only electronic configurations of these $S = 7/2$ ions (orbital angular momentum $L = 0$). The questions we wanted to address were how repeatable the large μ_{eff} is in different samples, how it comes about, and to see if it correlates with other properties of the material. In addition, we wanted to test our unified molecular field theory to fit the magnetic and thermal properties below T_N for another helical AFM to complement our earlier studies of

EuCo_2P_2 [43]. We grew single crystals of $\text{EuCo}_{2-y}\text{As}_2$ with two different fluxes and report their properties. We find that there is a rather large range of μ_{eff} values as well as of low-temperature ordered (saturation) moments μ_{sat} of the Eu spins in different crystals. As in $\text{CaCo}_{2-y}\text{As}_2$ [29, 30], we also find a significant ($\sim 5\%$) vacancy concentration on the Co sites in most of our $\text{EuCo}_{2-y}\text{As}_2$ crystals.

The experimental details are given in Sec. II. In Sec. III the crystal structure and composition analyses are presented for six crystals for which the physical properties are later studied in detail. Our magnetic susceptibility χ versus temperature T data and magnetization versus field $M(H)$ isotherms for the crystals are presented in Sec. IV, where we find enhancements in both μ_{eff} and μ_{sat} compared to expectation for Eu^{+2} spins with $S = 7/2$ and spectroscopic splitting factor $g = 2$. We also obtain an estimate of the amount of anisotropy in the system and fit the in-plane $\chi_{ab}(T)$ at temperatures T less than the AFM ordering temperature T_N by MFT.

Our zero-field and high-field heat capacity $C_p(H, T)$ measurements are presented in Sec. V, where the magnetic contribution $C_{\text{mag}}(T, H = 0)$ is extracted and found to agree rather well with the prediction of MFT for $S = 7/2$ at $T \leq T_N$. However, dynamic short-range AFM ordering is found from $T_N \approx 42$ K up to about 70 K, which is not accounted for by MFT. The molar magnetic entropy S_{mag} is found to agree with expectation for Eu spins $S = 7/2$ at high $T \gtrsim 70$ K, $R \ln(2S + 1)$, where R is the molar gas constant. From the high-field $C_p(H, T)$ we extract $T_N(H)$ for $H \parallel c$ and obtain a good fit by MFT. Using the high-field data from the $M(H)$ and $C_p(T)$ measurements, the phase diagrams in the $H \parallel c$ and $H \parallel ab$ versus T planes are constructed for two different crystals in Sec. VI. Electrical resistivity data for currents in the ab plane are presented in Sec. VII together with an analysis of these data in terms of the generic electron-electron scattering model at low T and the Bloch-Grüneisen, parallel-resistor, and s - d scattering models at higher T .

Our total-energy and electronic-structure calculations are presented in Sec. VIII. We find that the Eu spins ferromagnetically polarize the spins of the electrons deriving from the Co $3d$ t_{2g} states near the Fermi level by an amount consistent with the observed enhancement of the Eu moments. The calculations also indicate that the Co atoms make no contribution to the helical structure, again consistent with experiment. In Sec. IX we extract the Heisenberg exchange interactions J_{ij} from the previously-presented MFT fit to the $\chi_{ab}(T \leq T_N)$ data. A summary of our results is given in Sec. X.

II. EXPERIMENTAL DETAILS

Single crystals of EuCo_2As_2 were grown in Sn flux and CoAs flux. The purity and sources of the elements used were Eu (Ames Lab), and Co (99.998%), As (99.999 99%)

and Sn (99.9999%) from Alfa Aesar. For some crystal growths, the Co powder was additionally heated under a flow of H_2 gas under a pressure of 12 bar at a temperature of 324 °C for 12 h to remove possible surface oxidation. At this H_2 pressure and temperature, negligible H is absorbed by the Co [49]. Single crystals were grown in both Sn flux and CoAs flux using both H_2 -treated and as-received Co powder.

For Sn-flux growth, the starting materials were mixed in the molar ratio Eu:Co:As:Sn = 1.05:2:2:15. Excess Eu was required in order to obtain crystals without impurity phases occluded on or embedded within the crystals. The mixture was placed in an alumina crucible and then sealed in a silica tube under high-purity argon gas. After prereacting the elements at 600 °C for 6 h, the mixtures were placed in a box furnace and heated to 1050 °C at a rate of 50 °C/h, held there for 20 h, and then cooled to 600 °C at a rate of 4 °C/h. At this temperature the molten Sn flux was decanted using a centrifuge. Shiny platelike crystals of area 4–80 mm² by \approx 0.4 mm thick were obtained.

For CoAs-flux growth, a mixture of Eu metal and pre-reacted CoAs powder taken in the molar ratio Eu:CoAs = 1:4 which was placed in an alumina crucible and then sealed in a quartz tube under high purity argon gas. The tube assembly was placed in a box furnace and heated to 1300 °C at a rate of 50 °C/h, held there for 15 h, and then cooled to 1180 °C at a rate of 6 °C/h. At this temperature the excess CoAs flux was decanted using a centrifuge. For this crystal-growth method shiny plate-like crystals of size 4–40 mm² by 0.3–0.4 mm thick were obtained.

The phase purity and chemical composition of the $EuCo_2As_2$ crystals were checked using energy dispersive x-ray (EDX) semiquantitative chemical analysis attachment to a JEOL scanning electron microscope (SEM). SEM scans were taken on cleaved surfaces of the crystals which verified the single-phase nature of the crystals. The compositions of each side of a platelike crystal was measured at six or seven positions on each face, and the results were averaged. The EDX composition analysis revealed the presence of vacancies on the Co-site and an absence of Sn incorporated into the bulk of the crystals. The EDX data also showed no evidence for oxygen in any of the crystals. We selected six crystals having different Co-site occupancies for further investigations.

Single-crystal X-ray diffraction (XRD) measurements were performed at room temperature on a Bruker D8 Venture diffractometer operating at 50 kV and 1 mA equipped with a Photon 100 CMOS detector, a flat graphite monochromator and a Mo $K\alpha$ $I\mu S$ microfocus source ($\lambda = 0.71073$ Å). The raw frame data were collected using the Bruker APEX3 program [50], while the frames were integrated with the Bruker SAINT software package [51] using a narrow-frame algorithm for integration of the data and were corrected for absorption effects using the multiscan method (SADABS) [52]. The occupancies of the Co atomic sites were refined assuming ran-

dom occupancy of the Co sites and assuming complete occupancy of the Eu and As sites. The atomic thermal factors were refined anisotropically. Initial models of the crystal structures were first obtained with the program SHELXT-2014 [53] and refined using the program SHELXL-2014 [54] within the APEX3 software package.

Magnetization data were obtained using a Quantum Design, Inc., magnetic properties measurement system (MPMS) and a vibrating sample magnetometer in a Quantum Design, Inc., physical properties measurement system (PPMS) for high-field measurements up to 14 T, where 1 T \equiv 10⁴ Oe. The PPMS was used for $C_p(T)$ and $\rho(T)$ measurements. The $C_p(T)$ was measured by the relaxation method and the $\rho(T)$ using the standard four-probe ac technique.

III. CRYSTAL STRUCTURES AND COMPOSITIONS

The chemical compositions and crystallographic data are presented in Table I for six crystals of $EuCo_{2-y}As_2$ grown under different conditions with different Co vacancy concentrations as determined above, which are labeled #1 to #6, respectively. The chemical compositions obtained from the EDX and single crystal XRD analyses for these six crystals of $EuCo_2As_2$ are also listed in Table I in comparison with the previous studies on this compound [44–46, 48]. The physical property measurements reported in this paper were carried out on these six crystals.

IV. MAGNETIC SUSCEPTIBILITY AND HIGH-FIELD MAGNETIZATION

A. Magnetic Susceptibility

Figures 1 and 2 display the zero-field-cooled (ZFC) magnetic susceptibility $\chi \equiv M/H$ of Sn-flux-grown crystals and CoAs-flux-grown crystals, respectively, as a function of T with $H = 0.1$ T applied along the c axis (χ_c , $H \parallel c$) and in the ab plane (χ_{ab} , $H \parallel ab$). The T_N of a collinear AFM is given by the temperature of the maximum slope of χT versus T for the easy axis direction [55]; here, the corresponding field direction is within the easy ab plane of the helical magnetic structure. The inset of each figure shows $d(\chi_{ab}T)/dT$ versus T in the T range 2 to 100 K, with the peak temperature being T_N . The T_N obtained in this way for each crystal is shown in the insets of Figs. 1 and 2 as well as in Table I and in Table III below. From Table I one sees that the T_N values correlate with the crystallographic c/a ratio and with the flux used to grow the crystals, but not with the Co-site occupancy. The T_N values from previous reports on $EuCo_{2-y}As_2$ are also listed in Table I [44, 46, 47].

For all four crystals, from the main panels in Figs. 1 and 2 one sees that $\chi_{ab} > \chi_c$ in the paramagnetic

TABLE I: The compositions of our six $\text{EuCo}_{2-y}\text{As}_2$ single crystals, together with the error bars on the Co concentrations obtained from the combined EDX and XRD data, in comparison with previous studies on this compound. Also listed are crystallographic data for the single crystals at room temperature, including the fractional c -axis position z_{As} of the As site, the tetragonal lattice parameters a and c , the unit cell volume V_{cell} containing two formula units of $\text{EuCo}_{2-y}\text{As}_2$, and the c/a ratio. The AFM ordering temperature T_{N} are also shown. The listed values of the effective moment μ_{eff} obtained from the Curie constant in the Curie-Weiss law are averages of the c -axis and ab -plane values (see Table III below). Most values are larger than the value obtained for $S = 7/2$ and $g = 2$, which is $\mu_{\text{eff}} = 7.94 \mu_{\text{B}}/\text{Eu}$. The present work is denoted by PW. Data from the literature are also shown.

| Sample, Composition | z_{As} | a (Å) | c (Å) | V_{cell} (Å ³) | c/a | T_{N} (K) | μ_{eff} (μ_{B}/Eu) | Ref. |
|---|-----------------|------------|------------|--|-----------|-----------------------|--|------|
| #1 $\text{EuCo}_{1.90(1)}\text{As}_2^a$ | 0.3601(4) | 3.922(9) | 11.370(3) | 174.9(8) | 2.899(7) | 45.1(8) | 8.47 | PW |
| #2 $\text{EuCo}_{1.99(2)}\text{As}_2^b$ | 0.3611(5) | 3.910(5) | 11.306(9) | 172.8(6) | 2.891(6) | 44.9(5) | 8.62 | PW |
| #3 $\text{EuCo}_{1.92(4)}\text{As}_2^c$ | 0.3603(6) | 3.926(7) | 11.137(18) | 171.6(8) | 2.836(9) | 40.8(7) | 8.54 | PW |
| #4 $\text{EuCo}_{1.90(2)}\text{As}_2^d$ | 0.3607(1) | 3.9478(7) | 11.232(2) | 175.05(7) | 2.845(1) | 40.6(7) | 8.51 | PW |
| #5 $\text{EuCo}_{1.92(1)}\text{As}_2^d$ | 0.3623(2) | 3.9505(2) | 11.2257(7) | 175.19(2) | 2.8416(2) | 40.3(5) | 8.61 | PW |
| #6 $\text{EuCo}_{1.94(2)}\text{As}_2^a$ | 0.3683(3) | 3.9323(4) | 11.402(1) | 176.32(3) | 2.8996(5) | 45.8(3) | | PW |
| EuCo_2As_2 | | 3.964(2) | 11.111(6) | 174.6(2) | 2.803(3) | | | [45] |
| $\text{EuCo}_2\text{As}_2^e$ | | 3.934(1) | 11.511(6) | 178.1(2) | 2.926(2) | 47(2) | 7.4(1) | [46] |
| $\text{EuCo}_2\text{As}_2^d$ | 0.36 | 3.9671(1) | 11.0632(5) | 174.11(1) | 2.7887(2) | | | [48] |
| $\text{EuCo}_2\text{As}_2^f$ | 0.36109(5) | 3.929(1) | 11.512(4) | 177.7(1) | 2.930(2) | 47 | 8.00 ^g | [44] |
| $\text{EuCo}_2\text{As}_2^d$ | | | | | | 38.5 | 8.27 | [47] |

^aGrown in Sn flux

^bGrown in Sn flux with H₂-treated Co powder

^cGrown in CoAs flux with H₂-treated Co powder

^dGrown in CoAs flux

^ePolycrystalline sample

^fGrown in Bi flux

^gObtained by us by fitting the published $\chi(T)$ data

regime ($T > T_{\text{N}}$), indicating the presense of a magnetic anisotropy favoring the ab plane. This is consistent with the data for $T \ll T_{\text{N}}$ which indicates that the crystallographic ab -plane is an AFM easy plane. For $T < T_{\text{N}}$, one sees that χ_c is nearly independent of T , consistent with the molecular-field theory prediction for a field perpendicular to the ordering axis or plane of a Heisenberg AFM [56, 57]. Magnetocrystalline anisotropy determines the ordering axis or plane such as for a Heisenberg AFM with dipolar [58], uniaxial single-ion DS_z^2 [59], and classical field [60] anisotropies. The observation that χ_{ab} for $T \rightarrow 0$ is a large fraction of $\chi_c(T \rightarrow 0)$ indicates that $\text{EuCo}_{2-y}\text{As}_2$ is either a collinear AFM with multiple domains in the ab plane or a coplanar noncollinear ab plane AFM structure. The previous neutron diffraction study on EuCo_2As_2 indeed showed an incommensurate AFM helical structure in which Eu spins are aligned ferromagnetically within the ab plane, where the helix axis is the c -axis with an AFM propagation vector of $\mathbf{k} = (0, 0, 0.79)\pi/c$ where c is the tetragonal c -axis lattice parameter [44]. An incommensurate helical spin structure with almost the same propagation vector was found in the isostructural compound EuCo_2P_2 [40, 43].

The inverse susceptibility $\chi^{-1}(T)$ measured in $H = 0.1$ T applied along the c axis (χ_c^{-1}) and in the ab plane (χ_{ab}^{-1}) for Sn-flux- and CoAs-flux-grown crystals are shown in Figs. 3 and 4, respectively. As one can see from

the figures, the $\chi^{-1}(T)$ plots are slightly curved. One can fit this curvature by including a T -independent term χ_0 in addition to the Curie-Weiss law, giving a so-called modified Curie-Weiss law

$$\chi_\alpha = \chi_0 + \frac{C_\alpha}{T - \theta_{\text{p}\alpha}} \quad (\alpha = ab, c), \quad (1a)$$

where χ_0 is an isotropic temperature-independent term given by

$$\chi_0 = \chi^{\text{dia}} + \chi^{\text{para}} = \chi^{\text{core}} + \chi^{\text{Landau}} + \chi^{\text{Pauli}}, \quad (1b)$$

which is comprised of the diamagnetic (negative) atomic core (χ^{core}) and conduction-electron orbital Landau (χ^{Landau}) contributions and the paramagnetic (positive) contribution from the Pauli spin susceptibility (χ^{Pauli}) of the conduction electrons and/or holes. The Curie constant per mole of spins is given by [61]

$$C_\alpha = \frac{N_A g_\alpha^2 S(S+1) \mu_{\text{B}}^2}{3k_{\text{B}}} \equiv \frac{N_A \mu_{\text{eff}}^2 \mu_{\text{B}}^2}{3k_{\text{B}}}, \quad (1c)$$

where N_A is Avogadro's number and μ_{eff} is the "effective moment" of a spin in units of Bohr magnetons. From Eq. (1c) one obtains

$$\mu_{\text{eff}} = g \sqrt{S(S+1)} = \sqrt{\frac{3k_{\text{B}} C}{N_A \mu_{\text{B}}^2}}. \quad (1d)$$

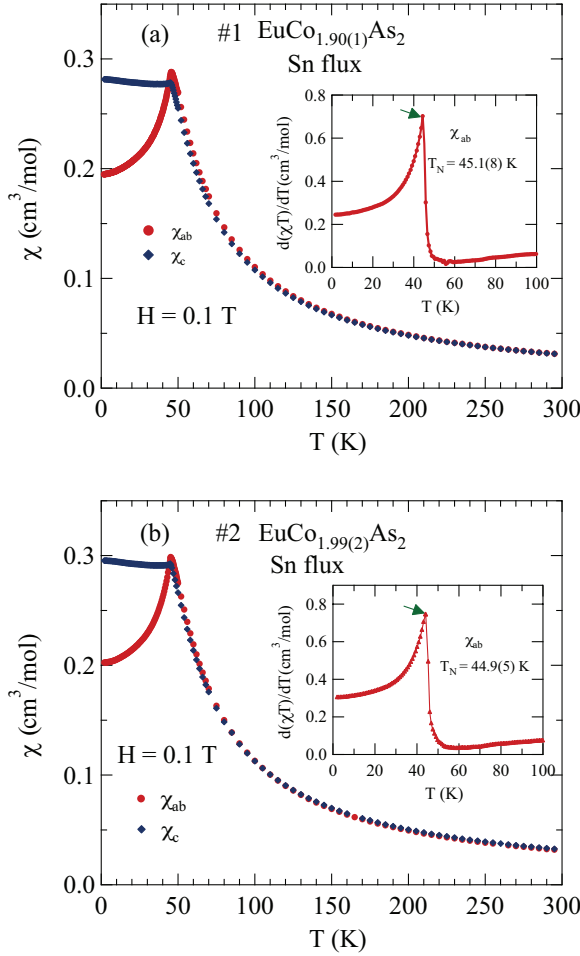


FIG. 1: Zero-field-cooled (ZFC) magnetic susceptibility $\chi \equiv M/H$ of Sn-flux-grown crystals (a) #1 $\text{EuCo}_{1.90(1)}\text{As}_2$ and (b) #2 $\text{EuCo}_{1.99(2)}\text{As}_2$ as a function of temperature T measured in magnetic fields $H = 0.1$ T applied in the ab plane (χ_{ab}) and along the c axis (χ_c). Insets: The respective derivative $d(\chi_{ab}T)/dT$ versus T .

Inserting the Gaussian cgs values of the fundamental constants into Eq. (1d) gives

$$\mu_{\text{eff}} \approx \sqrt{7.99684C} \approx \sqrt{8C}. \quad (1e)$$

As a baseline, we fitted the $\chi_\alpha(T)$ data by Eq. (1a) from 100 to 300 K with $\chi_0 = 0$ for each of five of our crystals for each of the two field directions, and the fitted C_α and $\theta_{p\alpha}$ values are shown in Table II together with μ_{eff} calculated from C using Eq. (1e). One sees that the values of μ_{eff} are 4% to 7% larger than the value for $S = 7/2$ with $g = 2$ given in the table caption, not including the data for outlier crystal #3. These differences are outside the experimental error of $\sim 1\%$. Our enhanced values of μ_{eff} are in qualitative agreement with the previous value in Table I reported in Ref. [47]. The positive values of $\theta_{p\alpha}$ indicate a net FM exchange interaction between the Eu^{+2} spins-7/2.

The value of $\theta_{p\alpha}$ obtained from a fit of experimental

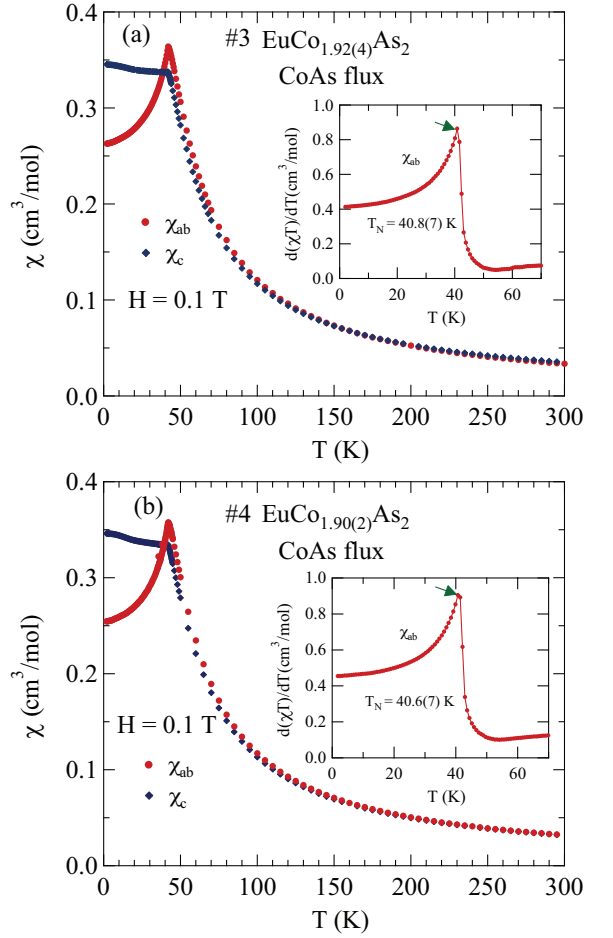


FIG. 2: Zero-field-cooled (ZFC) magnetic susceptibility $\chi \equiv M/H$ of CoAs-flux-grown crystals (a) #3 $\text{EuCo}_{1.92(4)}\text{As}_2$ and (b) #4 $\text{EuCo}_{1.90(2)}\text{As}_2$ versus temperature T measured in a magnetic field $H = 0.1$ T applied in the ab plane (χ_{ab}) and along the c axis (χ_c). Insets: The derivative $d(\chi_{ab}T)/dT$ versus T .

$\chi_\alpha(T)$ data in the paramagnetic regime at $T > T_N$ by Eq. (1a) can be affected by crystal-shape (demagnetization) effects if χ_α is large such as for compounds containing high concentrations of large-spin species such as Eu^{+2} with spin $S = 7/2$ in $\text{EuCo}_{2-y}\text{As}_2$. From the treatment in Ref. [58], for $\chi_0 = 0$ these affect the Weiss temperature according to

$$\theta_{p\alpha} = \theta_{p\alpha 0} - \frac{4\pi C_\alpha N_{d\alpha}}{V_M}, \quad (2a)$$

where $\theta_{p\alpha}$ is the fitted value as above, C_α is the Curie constant per mole of magnetic atoms, $\theta_{p\alpha 0}$ is the Weiss temperature that would have been obtained in the absence of demagnetization effects, $N_{d\alpha}$ is the magnetometric demagnetization factor in SI units ($0 \leq N_{d\alpha} \leq 1$) of a crystal with the applied field in the α direction, and V_M is the volume per mole of magnetic atoms in the crystal. For spins-7/2 with $g = 2$ one has isotropic $C_\alpha = 7.88 \text{ cm}^3 \text{ K/mol}$ and using the crystal data in Ta-

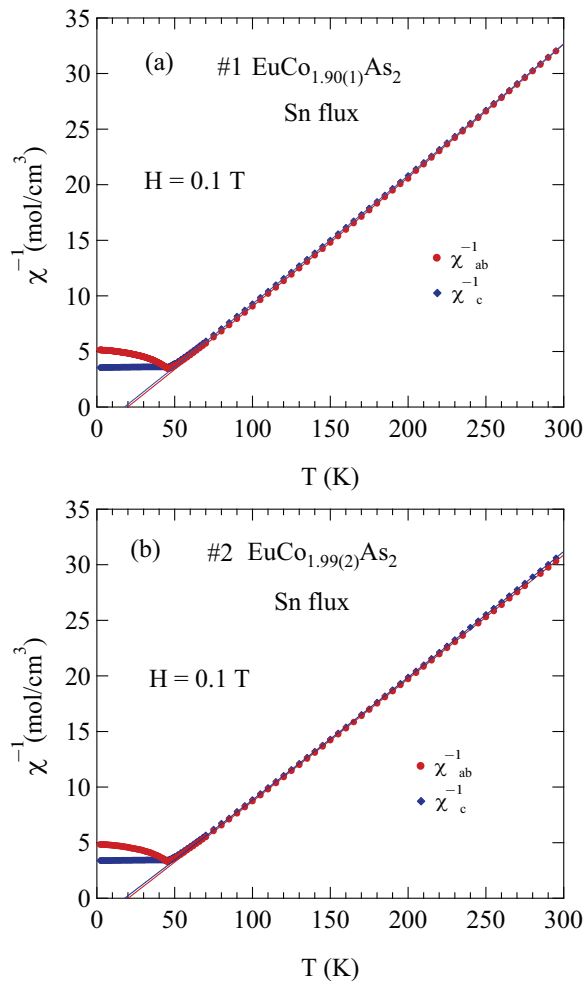


FIG. 3: (a) Inverse susceptibility χ^{-1} versus temperature T of Sn-flux-grown crystals (a) #1 $\text{EuCo}_{1.90(1)}\text{As}_2$ and (b) #2 $\text{EuCo}_{1.99(2)}\text{As}_2$ for $H = 0.1$ T applied in the ab plane ($H \parallel ab$, χ_{ab}^{-1}) and along the c axis ($H \parallel c$, χ_c^{-1}). The solid curves are fits by the modified Curie-Weiss law (1a) with parameters given in Table III.

ble I one obtains $V_M \approx 53 \text{ cm}^3/\text{mol}$ for $\text{EuCo}_{2-y}\text{As}_2$. Then for $\text{EuCo}_{2-y}\text{As}_2$, Eq. (2a) gives

$$\theta_{p\alpha} = \theta_{p\alpha 0} - (1.9 \text{ K})N_{d\alpha}. \quad (2b)$$

Since $0 \leq N_{d\alpha} \leq 1$, a fitted positive value of $\theta_{p\alpha}$ in Table II can thus be decreased by up to 1.9 K due to demagnetization effects, which is a maximum of $\sim 10\%$ of the $\theta_{p\alpha}$ values.

The data for C , μ_{eff} , and θ_p for crystal #3 in Table II are outliers. We infer that these erroneous values arise from the contribution of a small amount of a ferromagnetic impurity to the magnetization. In particular, including a χ_0 in the fits below yields a positive value that includes the FM impurity contribution and leads to C , μ_{eff} , and θ_p values in better alignment with those for the other four crystals. From the value of χ_0 obtained for crystal #3 below we estimate the contribution of the

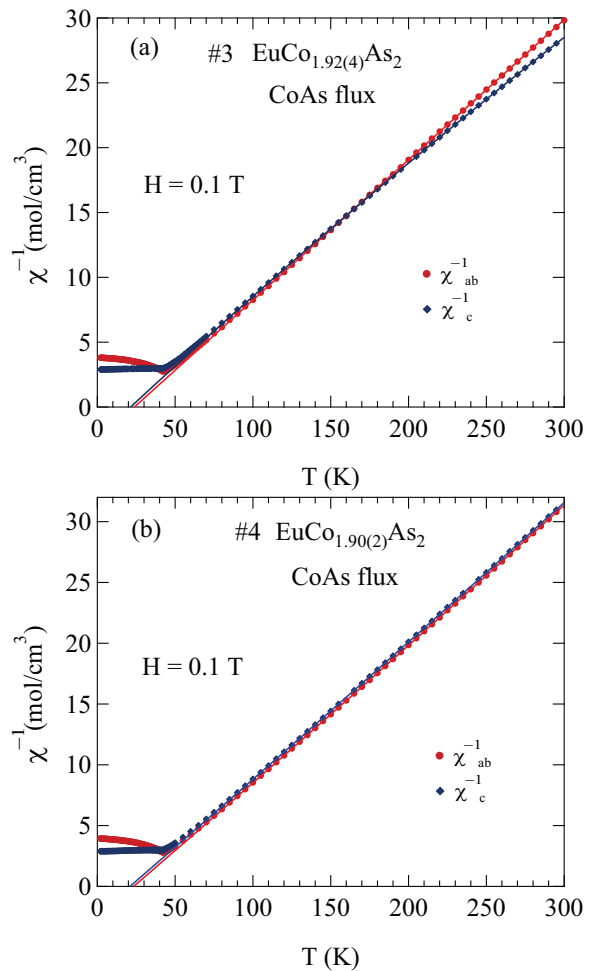


FIG. 4: (a) Inverse susceptibility χ^{-1} of CoAs-flux-grown crystals (a) $\text{EuCo}_{1.92(4)}\text{As}_2$ and (b) $\text{EuCo}_{1.90(2)}\text{As}_2$ as a function of temperature T for $H = 0.1$ T applied along the c axis ($H \parallel c$) and along the ab plane ($H \parallel ab$). The solid curves are fits by the modified Curie-Weiss law (1a) with parameters given in Table III.

FM impurity to the magnetization of the crystal in the measuring field of 0.1 T to be $\sim 5 \times 10^{-4} \mu_B/\text{f.u.}$

Next, we included χ_0 in the fits and the three fitting parameters are listed in Table III along with the previous reports for this compound. Most of the χ_0 values are strongly negative. The fits are shown as the solid curves in Figs. 3 and 4.

Now we obtain an estimate of χ_0 expected for EuCo_2As_2 . EuCo_2As_2 is not an ionic compound, so we do not use the ionic values [62] for the χ^{core} contributions. Instead, we use the atomic core contributions tabulated in Table 2.1 of Ref. [63], which are given per mole of atoms as

$$\chi^{\text{core}}(\text{Eu}) = -7.0 \times 10^{-5} \text{ cm}^3/\text{mol}, \quad (3a)$$

$$\chi^{\text{core}}(\text{Co}) = -3.1 \times 10^{-5} \text{ cm}^3/\text{mol}, \quad (3b)$$

$$\chi^{\text{core}}(\text{As}) = -3.3 \times 10^{-5} \text{ cm}^3/\text{mol}, \quad (3c)$$

TABLE II: Parameters obtained by fitting the $\chi(T)$ data in Figs. 1 and 2 for our crystals by Eq. (1a) assuming $\chi_0 = 0$. Shown for each crystal are the Curie constant C , Weiss temperature θ_p , and effective moment μ_{eff} obtained from C using Eq. (1d). For reference, for a spin $S = 7/2$ with $g = 2$, Eqs. (1a) and (1e) yield $C = 7.878 \text{ cm}^3 \text{ K/mol Eu}$ and $\mu_{\text{eff}} = 7.937 \mu_B/\text{Eu}$.

| Crystal | Field Direction | C ($\frac{\text{cm}^3 \text{ K}}{\text{mol}}$) | θ_p (K) | μ_{eff} (μ_B/Eu) |
|---|------------------|---|-------------------|---|
| #1 $\text{EuCo}_{1.90(1)}\text{As}_2^a$ | $H \parallel ab$ | 8.477(5) | 24.4(1) | 8.233 |
| | $H \parallel c$ | 8.543(4) | 21.66(9) | 8.265 |
| #2 $\text{EuCo}_{1.99(2)}\text{As}_2^b$ | $H \parallel ab$ | 9.020(2) | 21.81(4) | 8.493 |
| | $H \parallel c$ | 8.948(5) | 21.70(9) | 8.459 |
| #3 $\text{EuCo}_{1.92(4)}\text{As}_2^c$ | $H \parallel ab$ | 9.251(2) | 23.61(4) | 8.601 |
| | $H \parallel c$ | 10.01(1) | 12.6(2) | 8.947 |
| #4 $\text{EuCo}_{1.90(2)}\text{As}_2^d$ | $H \parallel ab$ | 8.753(3) | 26.05(7) | 8.366 |
| | $H \parallel c$ | 8.784(2) | 23.1(5) | 8.381 |
| #5 $\text{EuCo}_{1.92(1)}\text{As}_2^d$ | $H \parallel ab$ | 8.68(5) | 28.9(1) | 8.33 |
| | $H \parallel c$ | 8.97(1) | 27.2(1) | 8.47 |

^aGrown in Sn flux

^bGrown in Sn flux with H_2 -treated Co powder

^cGrown in CoAs flux with H_2 -treated Co powder

^dGrown in CoAs flux

yielding the core susceptibility per mole of EuCo_2As_2 as

$$\chi^{\text{core}}(\text{EuCo}_2\text{As}_2) = -1.98 \times 10^{-4} \text{ cm}^3/\text{mol}. \quad (3d)$$

Assuming the g factor of the conduction carriers is $g = 2$, the Pauli spin susceptibility of the conduction carriers in cgs units is given by

$$\chi^{\text{Pauli}} \left[\frac{\text{cm}^3}{\text{mol}} \right] = (3.233 \times 10^{-5}) \mathcal{D}(E_F) \left[\frac{\text{states}}{\text{eV f.u.}} \right], \quad (4)$$

where f.u. means the formula unit of $\text{EuCo}_{2-y}\text{As}_2$ and the density of states at the Fermi energy $\mathcal{D}(E_F)$ is for both spin directions, i.e., taking into account the Zeeman degeneracy of the conduction carriers. Taking $\mathcal{D}(E_F) \approx 7 \text{ states/eV f.u.}$ obtained from the $C_p(T)$ measurements in Table V below, one obtains

$$\chi^{\text{Pauli}} \approx 2.3 \times 10^{-4} \frac{\text{cm}^3}{\text{mol}}. \quad (5)$$

Then taking into account the Landau diamagnetism of the conduction carriers assuming a free-carrier gas gives the T -independent contribution to χ according to Eq. (1b) as

$$\chi_0 = \chi^{\text{core}} + \frac{2}{3} \chi^{\text{Pauli}} \approx -4.7 \times 10^{-5} \frac{\text{cm}^3}{\text{mol}}. \quad (6)$$

This value is much smaller in magnitude than the χ_0 values listed for crystals #1, #2, #4, and #5 in Table III, suggesting that these large negative values may instead

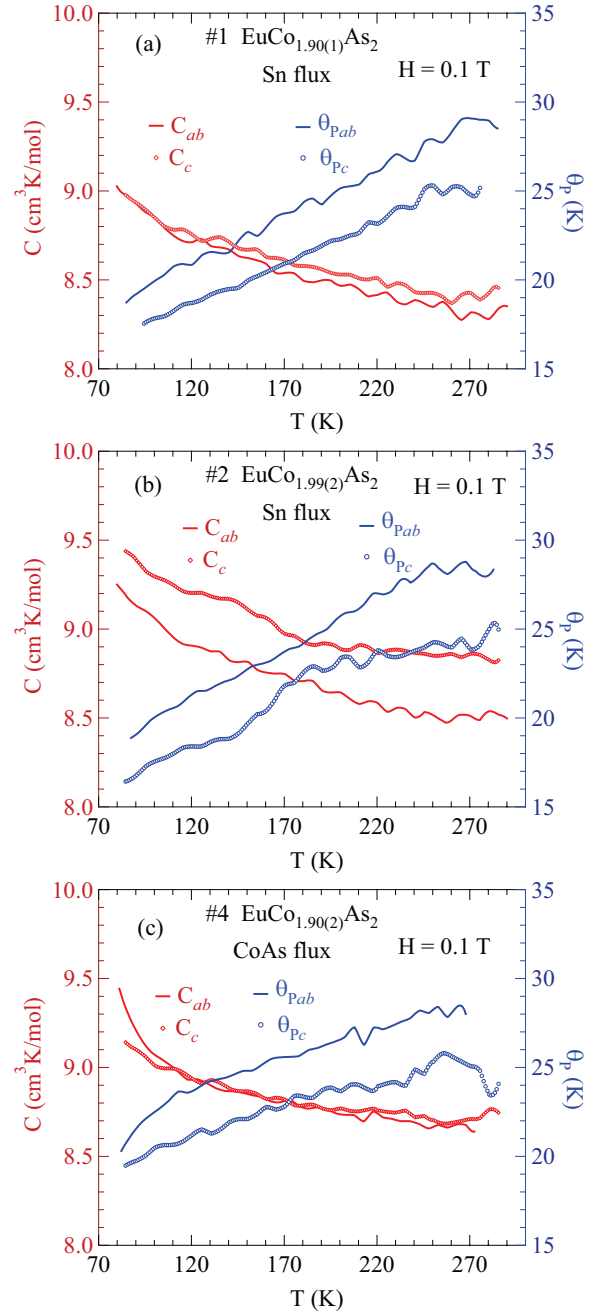


FIG. 5: Temperature T dependence of the Curie constant C_α and Weiss temperature $\theta_{p\alpha}$ of Sn-flux-grown crystals (a) #1 $\text{EuCo}_{1.90(1)}\text{As}_2$, (b) #2 $\text{EuCo}_{1.99(2)}\text{As}_2$, and (c) #4 $\text{EuCo}_{1.90(2)}\text{As}_2$, derived from Eqs. (7).

be reflections of T -dependent Curie constants and Weiss temperatures, a possibility examined next.

In order to investigate the possible T dependences of C_α and $\theta_{p\alpha}$, we again set $\chi_0 = 0$. We obtained a spline fit to $\chi_\alpha(T)$ from 70 to 300 K, and from that we obtained the temperature derivative $\chi'_\alpha(T)$. Then one has the two

simultaneous equations

$$\chi_\alpha(T) = \frac{C_\alpha}{T - \theta_{p\alpha}}, \quad (7a)$$

$$\chi'_\alpha(T) = -\frac{C_\alpha}{(T - \theta_{p\alpha})^2}, \quad (7b)$$

from which C_α and $\theta_{p\alpha}$ were solved for at each T . The results are shown in Fig. 5 for Sn-flux-grown crystals #1 $\text{EuCo}_{1.90(1)}\text{As}_2$ and #2 $\text{EuCo}_{1.99(4)}\text{As}_2$ and for CoAs-flux-grown crystal #4 $\text{EuCo}_{1.90(2)}\text{As}_2$. One sees smooth variations in C and θ_p versus T for each crystal, where C increases and θ_p decreases monotonically with decreasing T for each of the three crystals. This behavior of C might be expected if the Eu spins polarize the conduction electrons, since the polarization might be expected to increase with decreasing T .

The possibility of conduction-electron polarization due to progressive filling of the d band of the transition metal can lead to a variation of the asphericity of the valence shells of the Eu atoms through a weaker hybridization between the Eu valence states and Co d states. As a result, the itinerant electrons are strongly coupled to the localized moment, leading to an observed effective moment for an s -state Eu spin-7/2 given by [64]

$$\mu_{\text{eff}}^{\text{obs}} = \mu_{\text{eff}} \left[1 + \frac{2}{g} \rho_0(E_F) J_{sf} \right]. \quad (8)$$

Here we take $g = 2$, $\rho_0(E_F)$ is the density of states per atom at the Fermi surface for one spin direction, and J_{sf} is the effective sf exchange interaction due to either direct exchange (positive) or sf mixing (negative). The values of $\rho_0(E_F)J_{sf}$ estimated from the effective moments of $\text{EuCo}_{2-y}\text{As}_2$ compounds are given in the last column of Table III. The positive sign of the quantity suggests that the sf interaction mechanism in these compounds could be due to direct exchange. These interactions are expected to be affected by the change in lattice parameters a and c , and the overall unit-cell volume V_{cell} . Another possible reason for the excess Eu moment is related to the contribution of the non- $4f$ electrons of Eu, which is mainly from on-site $5d$ electrons. This gives rise to dressing of a bare rare-earth spin with a conduction electron spin cloud which for $\text{EuCo}_{2-y}\text{As}_2$ would add a portion of conduction-electron spin magnetization to the free electron moment. These effects are associated with the indirect RKKY (Ruderman-Kittel-Kasuya-Yosida) exchange interaction [65–67] and this may affect the g factor. Electron-spin resonance measurements may be useful to confirm or refute the hypothesis that the Curie constant changes with temperature as suggested in Fig. 5.

B. High-Field Magnetization

The T - and H -dependent magnetic susceptibility $\chi(T, H)$ was measured for one of the two crystals from

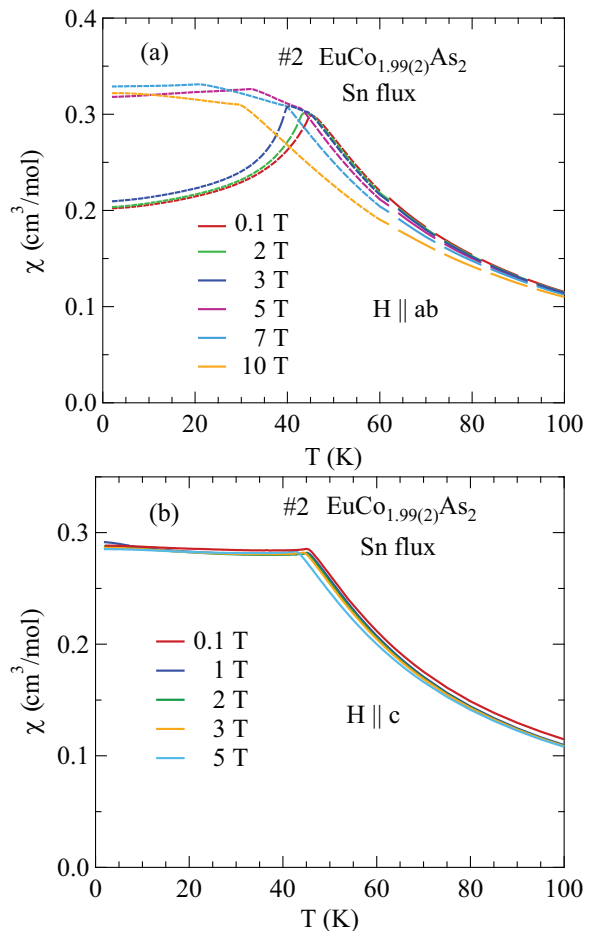


FIG. 6: Zero-field-cooled (ZFC) magnetic susceptibility $\chi \equiv M/H$ of Sn-flux-grown crystal #2 $\text{EuCo}_{1.99(2)}\text{As}_2$ as a function of temperature T for various magnetic fields H applied (a) in the ab plane (χ_{ab} , $H \parallel ab$) and (b) along the c axis (χ_c , $H \parallel c$).

each of the Sn-flux and CoAs-flux crystal growths. Figures 6 and 7 show $\chi(T)$ of Sn-flux-grown crystal #2 $\text{EuCo}_{1.99(2)}\text{As}_2$ and CoAs-flux-grown crystal #3 $\text{EuCo}_{1.92(4)}\text{As}_2$, respectively, for various values of H applied in the ab plane (χ_{ab} , $H \parallel ab$) and along the c axis (χ_c , $H \parallel c$) for $2 \text{ K} \leq T \leq 100 \text{ K}$. As shown in Figs. 6(a) and 7(a), the lowest- T data reveal a metamagnetic (MM) transition for $H \parallel ab$ between $H = 3 \text{ T}$ and 5 T . In addition, breaks in slope of $\chi(T)$ at each field are observed, signifying the H -dependent T_N which decreases with increasing H as expected for an AFM. Figures 6(b) and 7(b) show that T_N is much less sensitive to $H \parallel c$ than to $H \parallel ab$ as seen in Figs. 6(a) and 7(a).

Figures 8 and 9 show $M(H)$ isotherms at $T = 2 \text{ K}$ with H applied in the ab plane (M_{ab} , $H \parallel ab$) and along the c axis (M_c , $H \parallel c$) obtained for the Sn-flux-grown crystals #1 $\text{EuCo}_{1.90(1)}\text{As}_2$ and #2 $\text{EuCo}_{1.99(2)}\text{As}_2$ (Fig. 8), and for the CoAs-flux-grown crystals #3 $\text{EuCo}_{1.92(4)}\text{As}_2$ and #4 $\text{EuCo}_{1.90(2)}\text{As}_2$ (Fig. 9). The $M_c(H)$ data are nearly linear in field as predicted at $T \ll T_N$ by MFT for a

TABLE III: Parameters obtained from Modified Curie-Weiss fits of the magnetic susceptibility data between 100 and 300 K for $\text{EuCo}_{2-y}\text{As}_2$, where T_N is the Néel temperature, χ_0 is the T -independent contribution to the susceptibility, C_α is the molar Curie constant for fields in the $\alpha = ab, c$ direction, $\mu_{\text{eff}\alpha}$ is the effective moment, $\theta_{p\alpha}$ is the Weiss temperature, $\theta_{p\text{ave}}$ is the spherical average of $\theta_{p\alpha}$, $\rho_0(E_F)$ is the density of states at the Fermi energy per atom for one spin direction, and J_{sf} is the exchange interaction between a local f -electron atom and the s conduction electrons. For reference, the effective moment for Eu^{+2} with $g = 2$ and $S = 7/2$ is $\mu_{\text{eff}} = g\sqrt{S(S+1)}\mu_B = 7.94 \mu_B$. The quantity f_J is defined as $f_J = \theta_{p\text{ave}}/T_N$. PW means present work and N/A means not applicable.

| Compound | Ref. | Field Axis α | T_N (K) | χ_0 ($\frac{10^{-3} \text{cm}^3}{\text{mol}}$) | C_α ($\frac{\text{cm}^3 \text{K}}{\text{mol}}$) | $\mu_{\text{eff}\alpha}$ (μ_B/Eu) | $\theta_{p\alpha}$ (K) | $\theta_{p\text{ave}}$ (K) | $\rho_0(E_F)J_{sf}$ (K) | f_J |
|---|------|------------------------|--------------|--|---|---|---------------------------|-------------------------------|----------------------------|-------|
| #1 $\text{EuCo}_{1.90(1)}\text{As}_2^a$ | PW | H ab | 45.1(8) | -1.4(2) | 8.98(1) | 8.476(4) | 19.76(9) | 19.07 | 0.067 | 0.430 |
| | | H c | | -1.2(1) | 8.970(5) | 8.471(2) | 17.70(5) | | 0.0668 | |
| #2 $\text{EuCo}_{1.99(2)}\text{As}_2^b$ | PW | H ab | 44.9(5) | -0.54(1) | 9.214(3) | 8.585(1) | 20.10(3) | 19.33 | 0.081 | 0.441 |
| | | H c | | -1.2(3) | 9.38(1) | 8.662(4) | 17.8(1) | | 0.09 | |
| #3 $\text{EuCo}_{1.92(4)}\text{As}_2^c$ | PW | H ab | 40.8(7) | 0.07(3) | 9.23(1) | 8.593(5) | 23.8(1) | 22.99 | 0.08 | 0.563 |
| | | H c | | 2.75(2) | 9.005(6) | 8.488(3) | 21.38(6) | | 0.07 | |
| #4 $\text{EuCo}_{1.90(2)}\text{As}_2^d$ | PW | H ab | 40.6(7) | -0.87(1) | 9.062(5) | 8.514(2) | 23.33(4) | 22.54 | 0.072 | 0.555 |
| | | H c | | -0.68(1) | 9.028(5) | 8.498(2) | 20.97(5) | | 0.07 | |
| #5 $\text{EuCo}_{1.92(1)}\text{As}_2^d$ | PW | H ab | 40.3(5) | -1.33(6) | 9.15(2) | 8.556(9) | 24.9(2) | 24.23 | 0.077 | 0.601 |
| | | H c | | -1.45(3) | 9.48(1) | 8.708(4) | 22.9(1) | | 0.097 | |
| $\text{EuCo}_2\text{As}_2^d$ | [47] | H ab | 38.5 | 2.12 | 8.45 | 8.22 | 28.7 | 27.2 | 0.035 | 0.706 |
| | | H c | | -1.52 | 8.68 | 8.33 | 25.7 | | 0.049 | |
| $\text{EuCo}_2\text{As}_2^{e,f}$ | [44] | H ab | 47 | | 7.65(1) | 7.82(1) | 20.5(1) | 20.65 | 0.081 | 0.44 |
| | | H c | | | 8.39(1) | 8.19(1) | 20.8(3) | | 0.0025 | |
| $\text{EuCo}_2\text{As}_2^g$ | [46] | N/A | 47(2) | | | 7.4(1) | 18(4) | 18 | | 0.38 |

^aGrown in Sn flux

^bGrown in Sn flux with H₂-treated Co powder

^cGrown in CoAs flux with H₂-treated Co powder

^dGrown in CoAs flux

^eGrown in Bi flux

^fThe data were sent to us by the authors and we fitted them by $\chi = C/(T - \theta)$ from 100 to 300 K

^gPoycrystalline sample

helix with the applied field along the helix axis, reaching saturation at the perpendicular critical field $H_{c\perp} \sim 10$ –15 T, depending on the sample and field direction.

The $M_{ab}(H)$ isotherms at $T = 2$ K in Figs. 8 and 9 show what appears to be a field-induced spin-flop (SF) transition at a field H_{SF} , with a small hysteresis [see inset of Fig. 8(a)]. The magnetic moment attains its saturation moment μ_{sat} at the critical field H_c which separates the AFM from the paramagnetic (PM) phases. An additional transition of unknown origin at a field H_{MM} is also seen, with $H_{\text{SF}} < H_{\text{MM}} < H_c$.

The detailed $M(H)$ isotherms at many temperatures from 2 K to 300 K of Sn-flux-grown crystals #1 $\text{EuCo}_{1.90(1)}\text{As}_2$ and #2 $\text{EuCo}_{1.99(2)}\text{As}_2$ are shown in Figs. 10 and 11, respectively, and those of CoAs-flux-grown crystals #3 $\text{EuCo}_{1.92(4)}\text{As}_2$ and #4 $\text{EuCo}_{1.90(2)}\text{As}_2$ are shown in Figs. 12 and 13, respectively, where parts (a) and (b) of each of the four figures are for $H \parallel ab$ (M_{ab}) and $H \parallel c$ (M_c), respectively. For the Sn-grown crystals, $M_c(H)$ data in Figs. 10(b) and 11(b) show a negative curvature between 40 and 60 K, but a proportional behaviour of $M_c(H)$ is eventually ob-

served at higher temperature ($T > 80$ K). On the other hand, $M_{ab}(H)$ in Figs. 10(a) and 11(a) show clear spin flop and metamagnetic transitions at H_{SF} and H_{MM} , respectively, for $T \ll 40$ K. These SF and MM transitions shift to lower field with increasing temperature. As shown in Figs. 12 and 13, the CoAs-flux-grown crystals exhibit similar behaviors.

The transition fields H_{SF} , H_{MM} and H_c versus temperature are taken to be the fields at which dM/dH versus H exhibits a peak or a discontinuity (shown in Fig. 14 for Sn-flux-grown crystals and Fig. 15 for CoAs-flux-grown crystals). The results are listed in Table IV. One sees that $H_{c\parallel}$ is different from $H_{c\perp}$ and the saturation moments of these crystals are larger than the theoretical Eu^{+2} value $\mu_{\text{sat}} = gS\mu_B/\text{Eu} = 7 \mu_B/\text{Eu}$, where $g = 2$ and $S = 7/2$. As seen later in Sec. VIII, this enhancement is due to d -electron spin polarization by the ordered Eu spins.

TABLE IV: Spin-flop transition field H_{SF} , metamagnetic transition field H_{MM} , critical field H_c , and saturation moment μ_{sat} at $T = 2$ K of EuCo_2As_2 single crystals determined from isothermal $M(H)$ data for fields $H \parallel ab$ and $H \parallel c$.

| Crystal Designation | Field Direction | H_{SF} (T) | H_{MM} (T) | H_c (T) | μ_{sat} (μ_{B}/Eu) |
|---|------------------|---------------------|---------------------|-----------|---|
| #1 $\text{EuCo}_{1.90(1)}\text{As}_2^a$ | $H \parallel ab$ | 4.75 | 8.46 | 13.04 | 7.15 |
| | $H \parallel c$ | | | 13.32 | 7.05 |
| #2 $\text{EuCo}_{1.99(2)}\text{As}_2^b$ | $H \parallel ab$ | 4.8 | 8.2 | 12.8 | 7.03 |
| | $H \parallel c$ | | | 13.7 | 7.05 |
| #3 $\text{EuCo}_{1.92(4)}\text{As}_2^c$ | $H \parallel ab$ | 3.9 | 4.5 | 8.78 | 7.59 |
| | $H \parallel c$ | | | 9.9 | 7.57 |
| #4 $\text{EuCo}_{1.90(2)}\text{As}_2^d$ | $H \parallel ab$ | 3.8 | 4.6 | 9.5 | 7.34 |
| | $H \parallel c$ | | | 10.86 | 7.19 |
| #5 $\text{EuCo}_{1.92(1)}\text{As}_2^d$ | $H \parallel ab$ | 3.86 | 4.47 | 8.75 | 7.50 |
| | $H \parallel c$ | | | 9.96 | 7.58 |

^aGrown in Sn flux

^bGrown in Sn flux with H_2 -treated Co powder

^cGrown in CoAs flux with H_2 -treated Co powder

^dGrown in CoAs flux

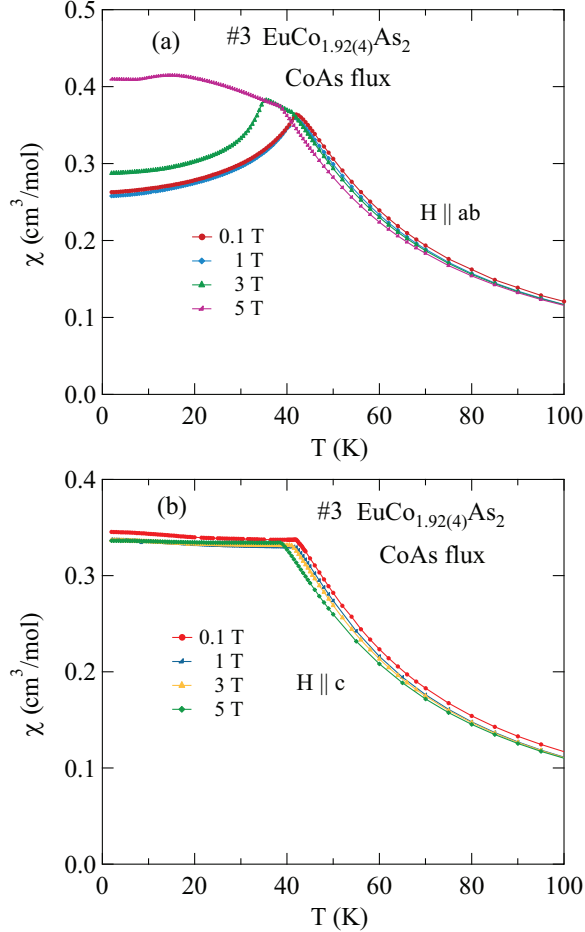


FIG. 7: Same as Fig. 6 except that the crystal measured is CoAs-flux-grown crystal #3 $\text{EuCo}_{1.92(4)}\text{As}_2$.

C. Influence of Anisotropy on the Magnetic Properties

From the above magnetic susceptibility and magnetization data, it is clear that magnetic anisotropy has an important influence on the results. For example, without anisotropy the spin-flop phase for fields in the ab plane would be the stable phase for all fields less than H_c . Here the anisotropy must give rise to an easy ab plane (XY anisotropy) because the helix axis is c axis and the moments are ferromagnetically-aligned within a given ab plane.

Here we estimate the strength of the anisotropy in terms of a generic classical anisotropy field. The formulas used here are derived in Ref. [60]. From the value of the anisotropy field parameter h_{A1} to be defined below, we estimate the influence of the anisotropy on the Néel temperature that would occur in the absence of anisotropy.

The definitions and predictions for this type of anisotropy in the presence of Heisenberg exchange interactions are given in Ref. [60] for systems comprised of identical crystallographically-equivalent spins as applies to the Eu sublattice in $\text{EuCo}_{2-y}\text{As}_2$. The XY anisotropy field \mathbf{H}_{Ai} seen by given moment $\vec{\mu}_i$ making an angle ϕ_i with the positive x axis (a axis here, where the z axis is the c axis) is given by an amplitude H_{A0i} times the projection of the moment onto the xy plane, i.e.,

$$\mathbf{H}_{Ai} = H_{A0i} \sin \theta_i (\cos \phi_i \hat{\mathbf{i}} - \sin \phi_i \hat{\mathbf{j}}). \quad (9)$$

The amplitude is expressed in terms of a more fundamental anisotropy field H_{A1} as

$$H_{A0i}(T) = \frac{3H_{A1}}{S+1} \bar{\mu}_i(T), \quad (10)$$

where the reduced ordered and/or field-induced mo-

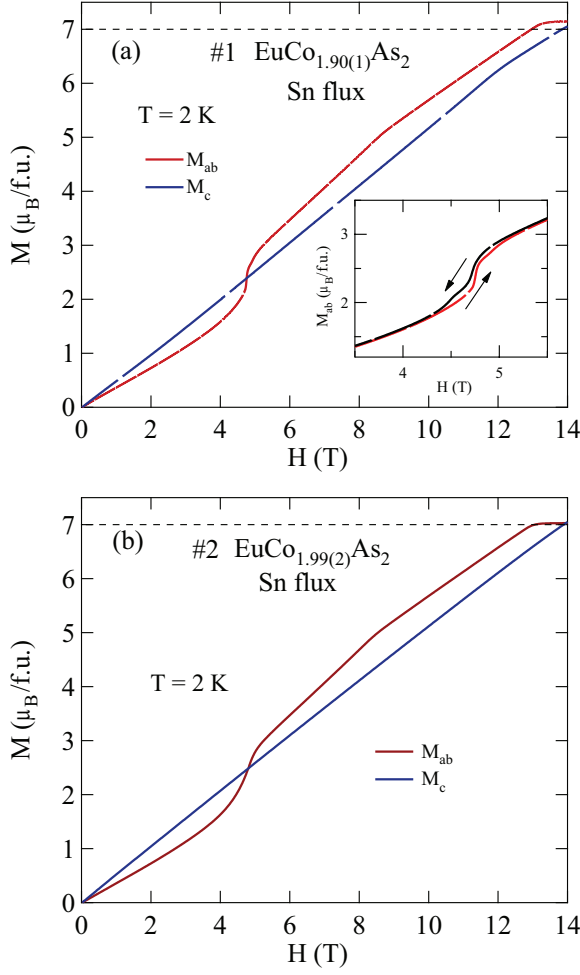


FIG. 8: Isothermal magnetization M of Sn-flux-grown crystals (a) #1 $\text{EuCo}_{1.90(1)}\text{As}_2$ and (b) #2 $\text{EuCo}_{1.99(2)}\text{As}_2$ as a function of applied magnetic field H measured at 2 K for H applied in the ab plane (M_{ab} , $H \parallel ab$) and along the c axis (M_c , $H \parallel c$).

ment $\bar{\mu}_i$ is

$$\bar{\mu}_i(T) \equiv \frac{\mu_i(T)}{\mu_{\text{sat}}} = \frac{\mu_i(T)}{g\mu_B S}, \quad (11)$$

where $\mu_i(T)$ is the T -dependent magnitude of $\bar{\mu}_i$. Finally, H_{A1} is expressed in reduced form h_{A1} as

$$h_{A1} = \frac{g\mu_B H_{A1}}{k_B T_{NJ}}, \quad (12)$$

where T_{NJ} is the value that the Néel temperature would have been due to Heisenberg exchange interactions alone (in the absence of anisotropy). Another parameter of the theory is

$$f_J = \frac{\theta_{pJ}}{T_{NJ}}, \quad (13)$$

where θ_{pJ} is the Weiss temperature in the Curie-Weiss law due to exchange interactions alone.

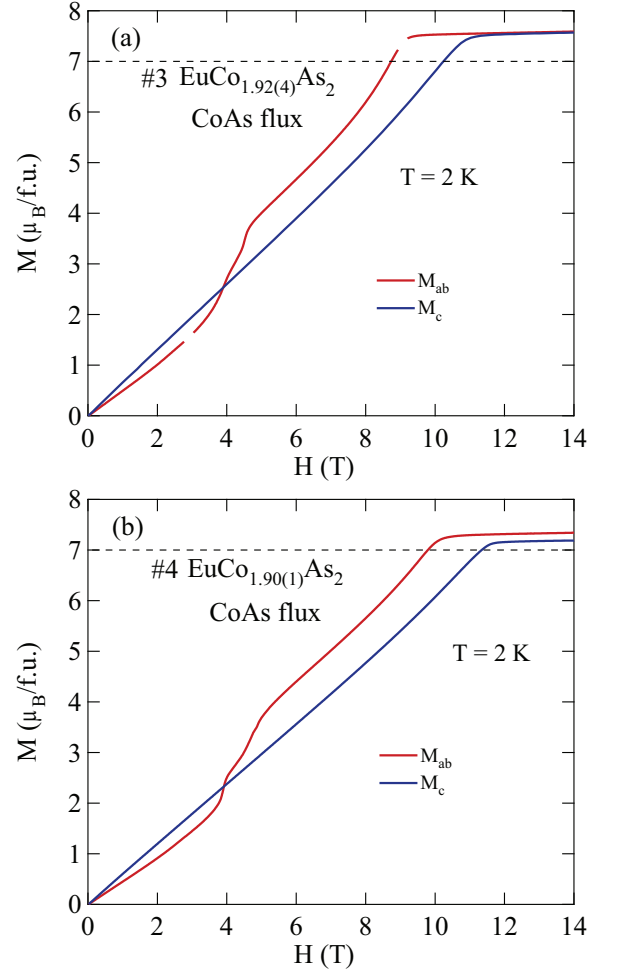


FIG. 9: Isothermal magnetization M of CoAs-flux-grown crystals (a) #3 $\text{EuCo}_{1.92(4)}\text{As}_2$ and (b) #4 $\text{EuCo}_{1.90(2)}\text{As}_2$ as a function of applied magnetic field H at 2 K for H applied in the ab plane (M_{ab} , $H \parallel ab$) and along the c axis (M_c , $H \parallel c$).

The Néel temperature T_N in $H = 0$ in the presence of both exchange and anisotropy fields is increased in the presence of the XY anisotropy field, as expected, according to the linear relation

$$T_N = T_{NJ}(1 + h_{A1}). \quad (14)$$

The anisotropic Weiss temperatures in the Curie-Weiss law for the paramagnetic susceptibility with XY anisotropy are

$$\theta_{pz} = \theta_{pJ}, \quad (15a)$$

$$\theta_{pxy} = \theta_{pJ} + T_{NJ}h_{A1}, \quad (15b)$$

$$\theta_{pxy} - \theta_{pz} = T_{NJ}h_{A1} = \frac{T_N h_{A1}}{1 + h_{A1}}, \quad (15c)$$

$$\frac{\theta_{pxy} - \theta_{pz}}{T_N} = \frac{h_{A1}}{1 + h_{A1}}, \quad (15d)$$

where we used Eq. (14) to obtain the third equality. This allows one to easily determine the parameter h_{A1} . Usually the ratio on the left side of Eq. (15d) is small, so one

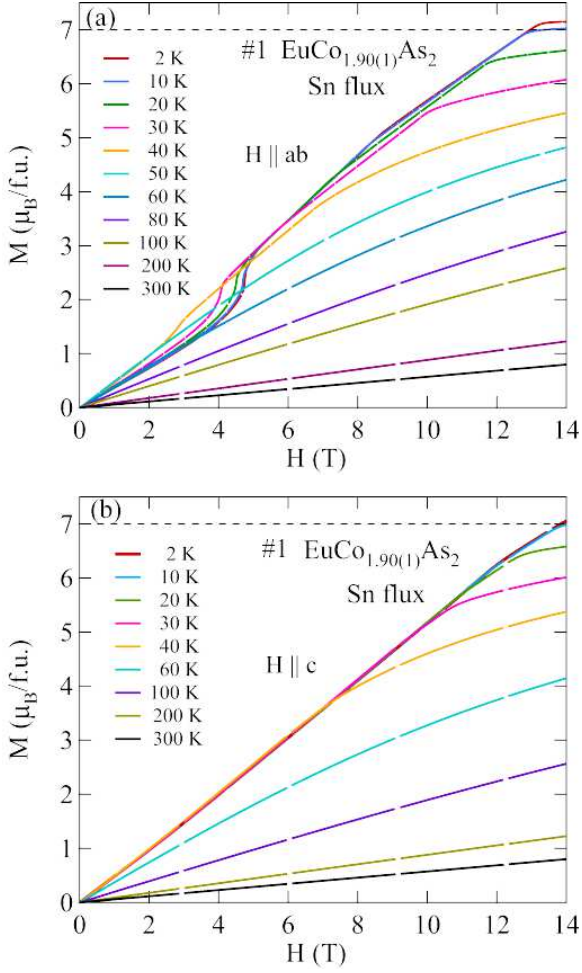


FIG. 10: Isothermal magnetization M of Sn-flux-grown crystal #1 $\text{EuCo}_{1.90(1)}\text{As}_2$ as a function of magnetic field H at the indicated temperatures for H applied (a) in the ab plane (M_{ab} , $H \parallel ab$) and (b) along the c axis (M_c , $H \parallel c$).

can instead use

$$\frac{\theta_{pxy} - \theta_{pz}}{T_N} \approx h_{A1} \quad (h_{A1} \ll 1), \quad (16)$$

which is equivalent to the approximation $T_N \approx T_{NJ}$. Using the T_N and $\theta_{pab} - \theta_{pc}$ values in Table III, one obtains

$$h_{A1} \approx 0.05 \text{ for } \text{EuCo}_{2-y}\text{As}_2. \quad (17)$$

Thus the XY anisotropy increases the Néel temperature, also θ_{pab} by about 5%, or about 2 K for $\text{EuCo}_{2-y}\text{As}_2$.

D. Fit of $\chi_{ab}(T \leq T_N)$ by Molecular Field Theory

In order to fit the low-field ab -plane susceptibility $\chi_{ab}(T \leq T_N)$ by the unified MFT for Heisenberg AFMs in Refs. [56] and [57], we assume that the Curie constant C_α and Weiss temperature $\theta_{p\alpha}$ ($\alpha = ab$ or c) in the PM state at $T \geq T_N$ are independent of T with the values given

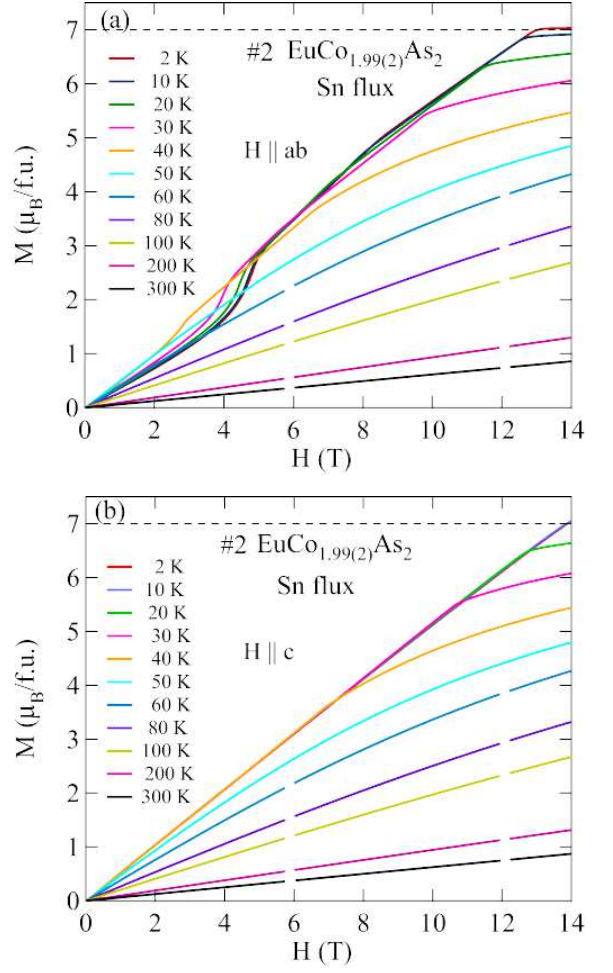


FIG. 11: Isothermal magnetization M of Sn-flux-grown crystal #2 $\text{EuCo}_{1.99(2)}\text{As}_2$ as a function of magnetic field H at the indicated temperatures for H applied (a) in the ab plane (M_{ab} , $H \parallel ab$) and (b) along the c axis (M_c , $H \parallel c$).

in Table III. We first remove the contributions of the T -independent susceptibility χ_0 and of anisotropy in the PM state to obtain the $\chi_{J\alpha}(T \geq T_N)$ that would have arisen from exchange interactions alone.

The T -independent susceptibility $\chi_{0\alpha}$ is taken into account at all temperatures according to

$$\chi_\alpha^*(T) = \chi_\alpha(T) - \chi_{0\alpha}, \quad (18)$$

where $\chi_\alpha(T)$ is the measured susceptibility and the $\chi_{0\alpha}$ values are given in Table III. We assume that the anisotropy in the PM state arises from sources such as magnetic dipole interactions and/or single-ion quantum uniaxial DS_z^2 anisotropy, for which the magnetic susceptibility tensor is traceless in the PM state [58, 59]. Then one obtains the Heisenberg susceptibility χ_J in the PM state given by

$$\chi_J(T \geq T_N) = \frac{1}{3} \left[2\chi_{ab}^*(T) + \chi_c^*(T) \right], \quad (19)$$

as shown in Fig. 16 for one each of the Sn-flux-grown and

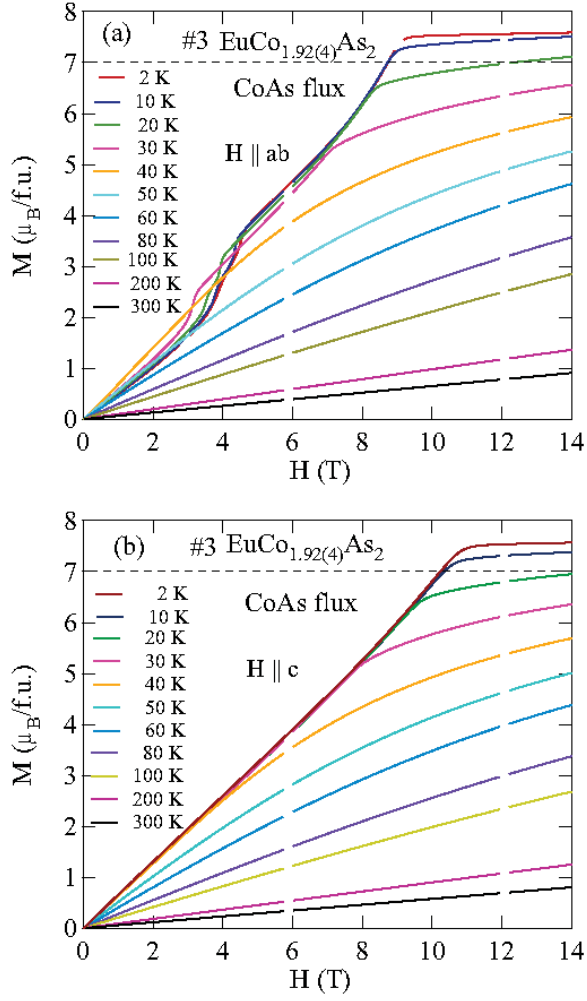


FIG. 12: (a) Isothermal magnetization M of CoAs-flux-grown crystal #3 $\text{EuCo}_{1.92(4)}\text{As}_2$ as a function of magnetic field H applied (a) in the ab plane ($H \parallel ab$) and (b) along the c axis ($H \parallel c$) at the indicated temperatures.

CoAs-flux grown crystals. As found above in Sec. IV C, the anisotropy increases T_N by about 5% and this small change will henceforth be ignored.

Within MFT, for $T \leq T_N$ the perpendicular susceptibility χ_{Jc} is predicted to be independent of T , in good agreement with the data in Fig. 16. The normalized $\chi_{Jab}(T \leq T_N)/\chi_J(T_N)$ for a helical Heisenberg AFM is given by [56, 57]

$$\frac{\chi_{Jab}(T \leq T_N)}{\chi_J(T_N)} = \frac{(1 + \tau^* + 2f_J + 4B^*)(1 - f_J)/2}{(\tau^* + B^*)(1 + B^*) - (f_J + B^*)^2}, \quad (20a)$$

where

$$B^* = 2(1 - f_J) \cos(kd) [1 + \cos(kd)] - f_J, \quad (20b)$$

$$t = \frac{T}{T_N}, \quad \tau^*(t) = \frac{(S+1)t}{3B'_S(y_0)}, \quad y_0 = \frac{3\bar{\mu}_0}{(S+1)t}, \quad (20c)$$

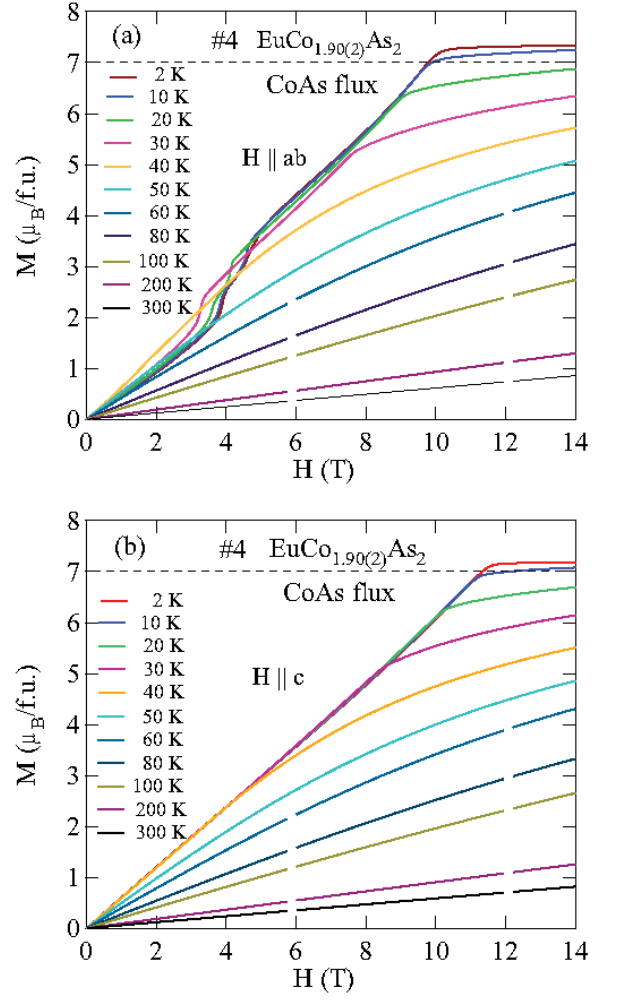


FIG. 13: (a) Isothermal magnetization M of CoAs-flux-grown crystal #4 $\text{EuCo}_{1.90(2)}\text{As}_2$ as a function of magnetic field H applied (a) in the ab plane ($H \parallel ab$) and (b) along the c axis ($H \parallel c$) at the indicated temperatures.

the ordered moment versus T in $H = 0$ is denoted by μ_0 , the reduced ordered moment $\bar{\mu}_0 = \mu_0/\mu_{\text{sat}}$ is determined by numerically solving the self-consistency equation

$$\bar{\mu}_0 = B_S(y_0), \quad (21)$$

$B'_S(y_0) = [dB_S(y)/dy]|_{y=y_0}$ and our definition of the Brillouin function $B_S(y)$ is given in Refs. [56] and [57].

We fitted the in-plane $\chi_{Jab}(T)$ data in Fig. 16 by Eqs. (20) using $S = 7/2$ and the indicated f_J values. For $kd(T)$ we used the neutron diffraction value $kd(T = 47 \text{ K}) = 0.79\pi$ [44]. In order to fit the lowest- T data, we used $kd(T = 0) = 0.82\pi$ for the Sn-flux-grown crystal and 0.798π for the CoAs-flux-grown crystal, calculated from Eqs. (20), which are comparable to the experimentally observed value with respect to neutron diffraction studies [44]. A rough estimated value of f_J is $f_J \sim (20 \text{ K})/(42 \text{ K}) \sim 0.5$. We treated f_J as an adjustable parameter. The $\chi_{Jab}(T \leq T_N)$ fits thus obtained are plotted as the solid blue curves in Figs. 16(a) and 16(b). Also shown are the

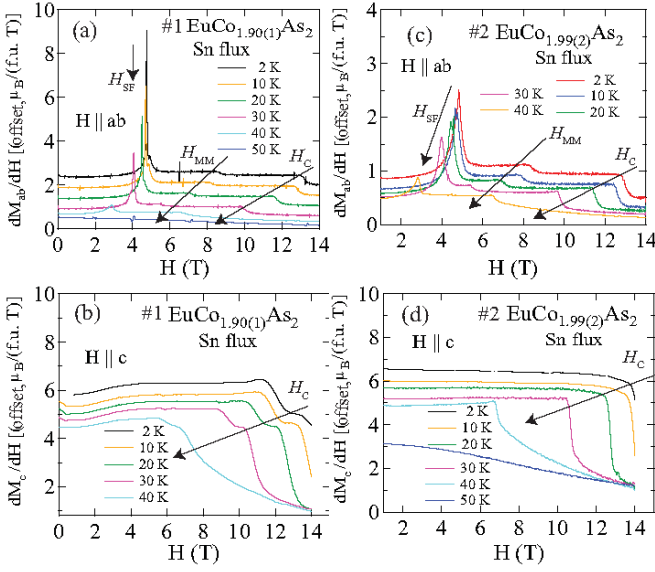


FIG. 14: Derivative dM/dH versus H for Sn-flux-grown crystals #1 $\text{EuCo}_{1.90(1)}\text{As}_2$ [(a) $H \parallel ab$, (b) $H \parallel c$] and #2 $\text{EuCo}_{1.99(2)}\text{As}_2$ [(c) $H \parallel ab$, (d) $H \parallel c$] for several temperatures T as indicated.

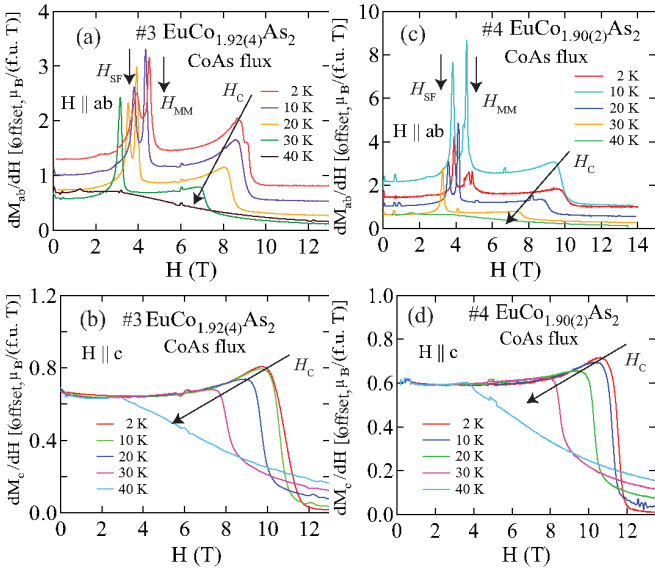


FIG. 15: Derivative dM/dH versus H of CoAs-flux-grown crystals #3 $\text{EuCo}_{1.92}\text{As}_2$ [(a) $H \parallel ab$, (b) $H \parallel c$] and #4 $\text{EuCo}_{1.90}\text{As}_2$ [(c) $H \parallel ab$, (d) $H \parallel c$] for several temperatures as indicated.

$\chi_{Jab}(T \leq T_N)$ curves using the approximate measured values of f_J . The discrepancy between the two fitted curves in each figure is a measure of the deficiency of MFT in predicting $\chi_{Jab}(T)$, as previously pointed out in Ref. [57].

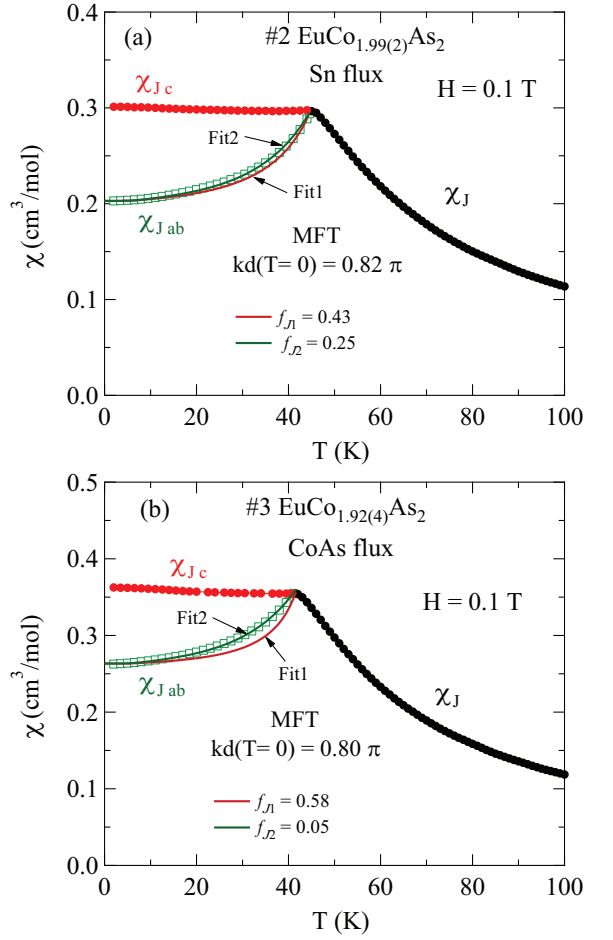


FIG. 16: $\chi_J(T)$ versus T for $H \parallel ab$ and $H \parallel c$ in $H = 0.1$ T for (a) Sn-flux-grown crystal #2 $\text{EuCo}_{1.99(2)}\text{As}_2$ and (b) CoAs-flux-grown crystal #3 $\text{EuCo}_{1.92(4)}\text{As}_2$. The fits of $\chi_{Jab}(T)$ for $T \leq T_N$ by the MFT prediction for a helix in Eqs. (20) are shown as the solid curves.

V. HEAT CAPACITY

A. Zero-Field Heat Capacity

The heat capacities $C_p(T)$ for Sn-flux-grown crystal #2 $\text{EuCo}_{1.99(2)}\text{As}_2$, CoAs-flux-grown crystal #3 $\text{EuCo}_{1.92(4)}\text{As}_2$, and the nonmagnetic reference compound BaCo_2As_2 [43] measured in the temperature range from 1.8 to 300 K are shown in Fig. 17. The data exhibit a prominent peak at $T_N = 45.1(2)$ K and $T_N = 40.02(4)$ K for crystals #2 and #3, respectively. Low-temperature C_p/T vs T^2 plots in the range 1.8 to 5 K for the above two crystals and for Sn-flux-grown crystal #6 $\text{EuCo}_{1.94(2)}\text{As}_2$ are shown in the insets of Fig. 17. The data for all three crystals exhibit negative curvature below ~ 3 K and hence cannot be fitted by the conventional expression [61]

$$\frac{C_p(T)}{T} = \gamma + \beta T^2, \quad (22)$$

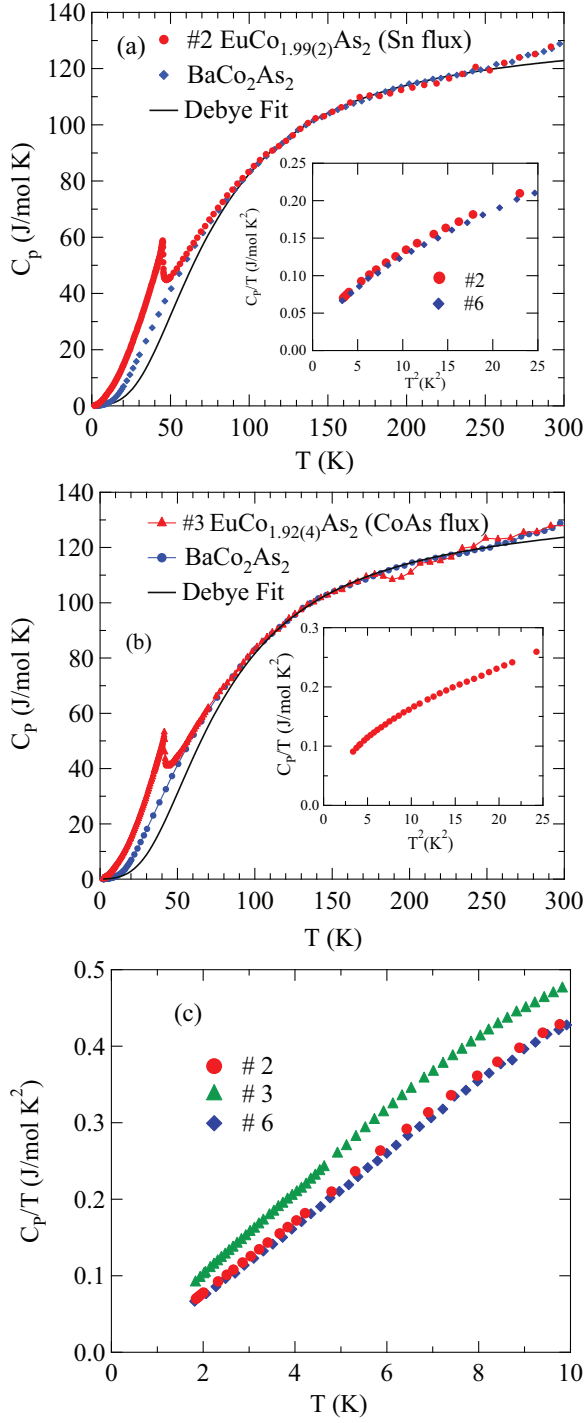


FIG. 17: Temperature dependence of the heat capacity $C_p(T)$ in $H = 0$ for (a) Sn-flux-grown #2 $\text{EuCo}_{1.99(2)}\text{As}_2$ and (b) CoAs-flux-grown #3 $\text{EuCo}_{1.92(4)}\text{As}_2$ crystals. Both panels also show $C_p(T)$ of the nonmagnetic reference compound BaCo_2As_2 [43]. The black curves are Debye lattice heat capacity model fits to the data between 100 and 280–300 K by Eq. (23). Insets: C_p/T versus T^2 for the three crystals #2, #3, and Sn-flux-grown #6 $\text{EuCo}_{1.94(2)}\text{As}_2$. The data do not follow the behavior expected from Eq. (22). (c) Plots of $C_p(T)/T$ versus T .

TABLE V: Parameters γ and β obtained for pnictide compounds isostructural to $\text{EuCo}_{2-y}\text{As}_2$. Also listed are the Debye temperatures Θ_D obtained from β according to Eq. (25) and the density of states at the Fermi energy $D_\gamma(E_F)$ obtained from γ via Eq. (24b). Values of γ and Θ_D for both $\text{EuCo}_{1.99(2)}\text{As}_2$ and $\text{EuCo}_{1.92(4)}\text{As}_2$ are obtained by fitting the $C_p(T)$ data between 100 and 280 K in Fig. 17 by the Debye model plus a γT term according to Eq. (23).

| Crystal | γ ($\frac{\text{mJ}}{\text{mol K}^2}$) | β ($\frac{\text{mJ}}{\text{mol K}^4}$) | Θ_D (K) | $D_\gamma(E_F)$ ($\frac{\text{states}}{\text{eV f.u.}}$) |
|--|--|---|---------------------|---|
| #2 $\text{EuCo}_{1.99(2)}\text{As}_2$ ^{a,c} | 15(2) | 0.33(1) | 308(3) | 6.3(8) |
| #3 $\text{EuCo}_{1.92(4)}\text{As}_2$ ^{b,c} | 18(3) | 0.31(1) | 314(4) | 7(1) |
| EuCo_2P_2 [43] | 23.7(5) | 2.8(1) | 151(2) | 10.0(2) |
| | | | 480(6) ^e | |
| BaCo_2P_2 [43] | 37.3(3) | 0.21(1) | 359(6) | 15.8(2) |
| SrCo_2P_2 [31] | 37.8(1) | 0.611(7) | 251(1) | 16.0(3) |
| BaCo_2As_2 ^d [32] | 39.8(1) | 0.386(4) | 293(2) | 16.9(1) |
| $\text{CaCo}_{1.86}\text{As}_2$ ^d [29] | 27(1) | 1.00(8) | 212(1) | 11.4(5) |

^aGrown in Sn flux with H_2 -treated Co powder

^bGrown in CoAs flux with H_2 -treated Co powder

^cFrom a 100–280 K fit of $C_p(T)$ by Eq. (23)

^dGrown in Sn flux

^eFrom a 200–280 K fit of $C_p(T)$ by Eq. (23)

where γ is the Sommerfeld coefficient associated with the conduction electrons and β is the coefficient of the T^3 lattice and three-dimensional AFM spin-wave contributions. Below we attempt to find γ by fitting the high- T data. In Table V are shown data obtained for similar isostructural compounds.

Shown in Fig. 17(c) are plots of $C_p(T)/T$ versus T for the three crystals #2, #3, and #6. One sees that each crystal shows approximately linear behavior over the T range from 3 to 6 K, i.e., that C_p has an approximately T^2 contribution over this T range. From preliminary linear spin-wave calculations, this behavior may arise from the temperature-dependent heat capacity of AFM spin waves.

The $C_p(T)$ data for our crystals in the temperature range $120 \text{ K} \leq T \leq 280 \text{ K}$ are analysed using an electronic γT term plus the Debye model for the lattice heat capacity [61]

$$C_p(T) = \gamma T + nC_{V\text{Debye}}(T/\Theta_D), \quad (23)$$

$$C_{V\text{Debye}}(T/\Theta_D) = 9R \left(\frac{T}{\Theta_D} \right)^3 \int_0^{\Theta_D/T} \frac{x^4 e^x}{(e^x - 1)^2} dx,$$

The representation of the Debye function $C_{V\text{Debye}}(T/\Theta_D)$ used here is an accurate analytic Padé approximant function of T/Θ_D [68]. The fits to the $C_p(T)$ data over the temperature range 100 to 280 K by Eq. (23) are shown as the black solid curves in Figs. 17(a) and 17(b) and the fitted values of γ and Θ_D are listed in Table V.

The density of conduction carrier states at the Fermi

energy E_F , $D_\gamma(E_F)$, is obtained from γ according to [61]

$$D_\gamma(E_F) = \frac{3\gamma}{\pi^2 k_B^2}, \quad (24a)$$

which gives

$$D_\gamma(E_F) \left[\frac{\text{states}}{\text{eV f.u.}} \right] = \frac{1}{2.359} \gamma \left[\frac{\text{mJ}}{\text{mol K}^2} \right]. \quad (24b)$$

The $D_\gamma(E_F)$ values calculated for $\text{EuCo}_{2-y}\text{As}_2$ crystals #2 and #3 from their γ values using Eq. (24b) are listed in Table V, where values from the literature for similar compounds [29, 31, 32, 43] are also given.

The Debye temperature is estimated from the value of β in Eq. (22) from the expression [61]

$$\Theta_D = \left(\frac{12\pi^4 nR}{5\beta} \right)^{1/3}, \quad (25)$$

where n is the number of atoms per formula unit ($n = 5 - y$ for $\text{EuCo}_{2-y}\text{As}_2$) and R is the molar gas constant. The values of Θ_D obtained from the β values for other compounds [29, 31, 32, 43] are listed for comparison with those for our crystals in Table V.

The magnetic contribution $C_{\text{mag}}(T)$ to $C_p(T)$ for the $\text{EuCo}_{2-y}\text{As}_2$ crystals is obtained by subtracting $C_p(T)$ of the nonmagnetic reference compound BaCo_2As_2 from those of the $\text{EuCo}_{2-y}\text{As}_2$ crystals, as shown in Figs. 18(a) and 18(b), respectively. Within the Weiss MFT the discontinuity in the magnetic heat capacity at T_N for a spin $S = 7/2$ system is given by

$$\Delta C_{\text{mag}} = \frac{5RS(S+1)}{1+2S+2S^2} = 20.14 \text{ J/mol K}. \quad (26)$$

The jump in the heat capacity at T_N is ≈ 23.2 J/mol K and 21.74 J/mol K in the Sn-flux-grown crystal #2 $\text{EuCo}_{1.99(2)}\text{As}_2$ and the CoAs-flux-grown crystal #3 $\text{EuCo}_{1.92(4)}\text{As}_2$, respectively, which are somewhat larger than the prediction (26) of MFT. The discrepancy arises from the difference between the observed λ -shape and the predicted step-shape of $C_{\text{mag}}(T)$ at T_N . The nonzero contribution to $C_{\text{mag}}(T)$ for $T_N < T \lesssim 100$ K reflects the presence of dynamic short-range AFM ordering of the Eu spins above T_N . The hump in $C_{\text{mag}}(T)$ below T_N at $T \sim 15$ K arises naturally within MFT for large S [56]. The solid blue curves in Figs. 18(a) and 18(b) represent the MFT prediction for $C_{\text{mag}}(T)$ calculated for each respective T_N and for $S = 7/2$ which are in reasonable agreement with the data for each crystal below the respective T_N .

The magnetic entropy $S_{\text{mag}}(T)$ in $H = 0$ is calculated from the $C_{\text{mag}}(T)$ data for each crystal according to $S_{\text{mag}}(T) = \int_0^T [C_{\text{mag}}(T)/T] dT$ and the results are shown in Fig. 18(b) for Sn-flux-grown crystal #2 $\text{EuCo}_{1.99(2)}\text{As}_2$ and in Fig. 18(d) for CoAs-flux-grown crystal #3 $\text{EuCo}_{1.92(4)}\text{As}_2$. The horizontal dashed line in each figure is the theoretical high- T limit $S_{\text{mag}} = R \ln(2S+1) = 17.29$ J/mol K for $S = 7/2$. For each crystal, the entropy reaches $\approx 90\%$ of $R \ln(8)$ at T_N and recovers the full value by ~ 70 K.

B. High-Field Heat Capacity

Figures 19(a) and 20(a) show $C_p(H, T)$ for Sn-flux-grown crystal #2 $\text{EuCo}_{1.99(2)}\text{As}_2$ and CoAs-flux-grown crystal #3 $\text{EuCo}_{1.92(4)}\text{As}_2$, respectively, measured in various applied magnetic fields up to 9 T with $H \parallel c$. Thus the field direction is perpendicular to the ab plane of the ordered moments in $H = 0$ which we therefore denote as $H_\perp \equiv H \parallel c$ [56]. It is evident that the AFM transition temperature $T_N(H_\perp)$ shifts to lower temperature and that the heat capacity jump at $T_N(H_\perp)$ decreases with increasing field, both as predicted from MFT in Ref. [56] for a field parallel to the helix axis. The data in the $H - T$ phase diagrams with $H \parallel c$ in Figs. 19(b) and 20(b) were constructed from the H_\perp dependence of T_N obtained from the respective Figs. 19(a) and 20(a).

The MFT prediction for the critical field $H_{c\perp}(T)$ at which the AFM state undergoes a second-order transition to the PM state with increasing field at fixed T is given by [56]

$$H_{c\perp}(T) = H_{c\perp}(0) \bar{\mu}_0(T), \quad (27a)$$

where the reduced T -dependent ordered moment $\bar{\mu}_0(T)$ is obtained by solving Eq. (21) and the zero-temperature critical field is given by

$$H_{c\perp}(0) = \frac{3k_B T_N (1 - f_J)}{g \mu_B (S + 1)}. \quad (27b)$$

In convenient units where $H_{c\perp}(0)$ is expressed in Teslas ($1 \text{ T} \equiv 10^4 \text{ Oe}$) and taking $g = 2$ and $S = 7/2$ for Eu^{+2} , one has

$$H_{c\perp}(0)[\text{T}] = 0.4962(1 - f_J) T_N[\text{K}]. \quad (27c)$$

The values of T_N and f_J for the four crystals studied in this paper are given in Table III. For Sn-flux-grown crystal #2 $\text{EuCo}_{1.99(2)}\text{As}_2$, Eq. (27c) gives

$$H_{c\perp}(0) = 12.1 \text{ T}, \quad (28a)$$

and for CoAs-flux-grown crystal #3 $\text{EuCo}_{1.92(4)}\text{As}_2$, one obtains

$$H_{c\perp}(0) = 8.9 \text{ T}. \quad (28b)$$

These values have the same relationship to each other as do the critical fields H_c obtained from $M(H, T = 2 \text{ K})$ data that are listed in Table IV for $H \parallel c$.

Using $H_{c\perp}(0)$ as a fitting parameter, we fitted the $H_{c\perp}(T)$ data in Figs. 19(b) and 20(b) by Eq. (27a) and obtained $H_{c\perp}(0) = 14.8(4)$ T for crystal #2 and $H_{c\perp}(0) = 12.1(3)$ T for crystal #3. The fits are shown by the solid blue curves in Figs. 19(b) and 20(b), respectively.

VI. PHASE DIAGRAMS IN THE FIELD-TEMPERATURE PLANE

From the transitions observed in Figs. 6–15, 19, and 20, the phase diagrams in the $H - T$ plane were constructed

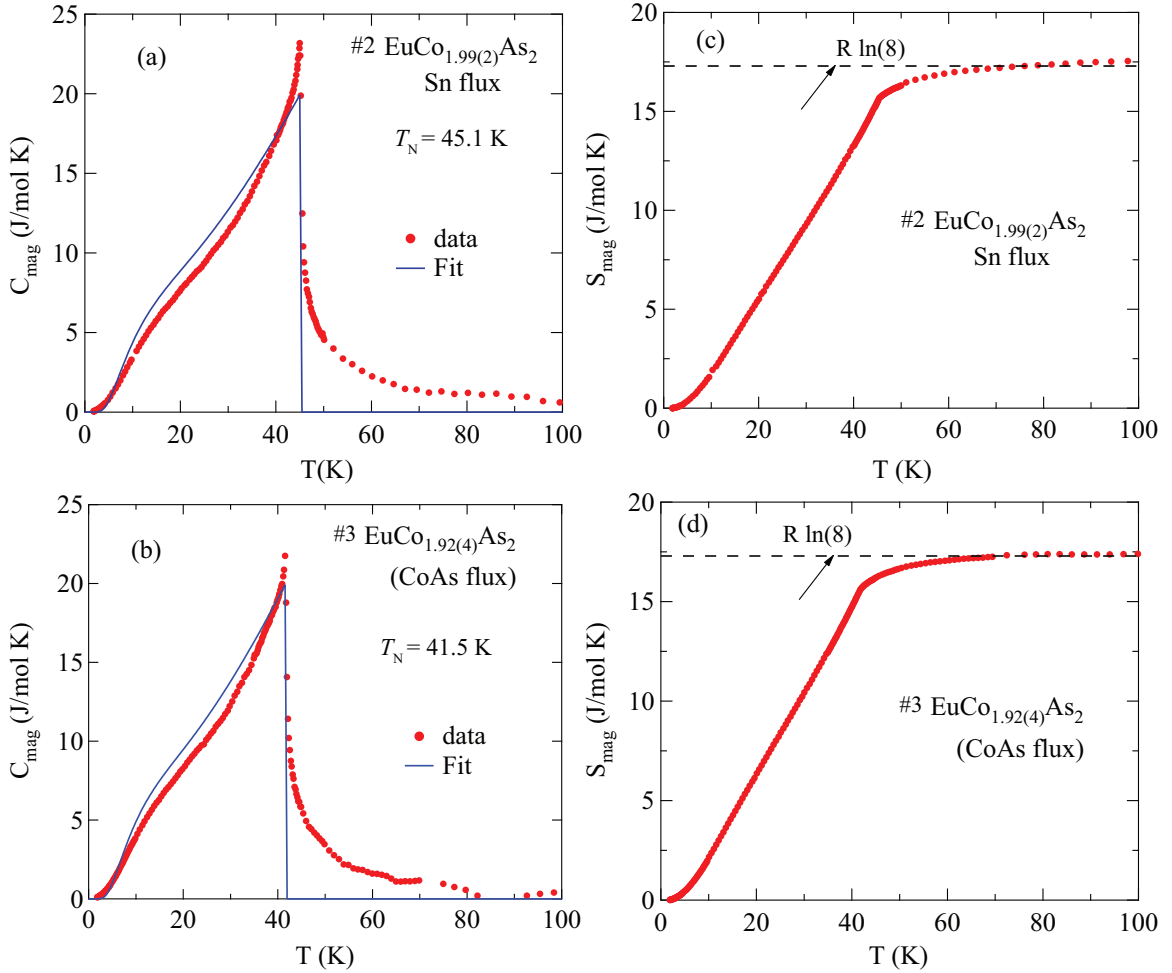


FIG. 18: Magnetic contributions $C_{\text{mag}}(T)$ and $S_{\text{mag}}(T)$ to the heat capacity and entropy, respectively, of (a,c) Sn-flux-grown crystal #2 $\text{EuCo}_{1.99(2)}\text{As}_2$ and (b,d) CoAs-flux-grown crystal #3 $\text{EuCo}_{1.92(4)}\text{As}_2$. In (c,d), the horizontal dashed line is the theoretical high- T limit $S_{\text{mag}} = R \ln(2S + 1) = 17.29$ J/mol K for Eu^{+2} with $S = 7/2$.

and are shown for Sn-flux-grown crystal #2 and CoAs-flux-grown crystal #3 in Figs. 21(a,b) and 21(c,d), each for both $H \parallel c$ and $H \parallel ab$. For $H \parallel c$, the observed phases are the AFM and PM phases, whereas for $H \parallel ab$, there are AFM, MM and PM phases. For $H \parallel c$ in Figs. 21(b,d), the only phase transition line is a second-order transition at the critical field H_c that separates the canted AFM phase from the PM phase. For $H \parallel ab$ in Figs. 21(a,c), there are three phase transition curves: (1) the first-order spin-flop transition at H_{SF} that separates the canted AFM and SF states; (2) a second-order intermediate metamagnetic transition at H_{MM} of unknown origin that separates SF and MM phases; and (3) the second-order critical field transition curve H_c that separates the MM and PM states.

VII. ELECTRICAL RESISTIVITY

A. Zero-Field Resistivity

The ab -plane electrical resistivity ρ as a function of temperature T from 1.8 to 320 K measured in $H = 0$ for Sn-flux-grown crystal #2 and CoAs-flux-grown crystal #3 are shown in Figs. 22(a) and 22(b), respectively. The $\rho(T)$ data for both crystals exhibit metallic behavior. For the Sn-flux-grown crystal #2, the residual resistivity is $\rho_0 = 12.0 \mu\Omega \text{ cm}$ at $T = 1.8$ K and the residual resistivity ratio is $\text{RRR} \equiv \rho(320 \text{ K})/\rho(1.8 \text{ K}) = 3.85$. As shown in the inset of Fig. 22(a), a slope change in $\rho(T)$ occurs at $T_N = 45.0(4)$ K, a value consistent with the T_N found from the above $C_p(T)$ and $\chi(T)$ measurements on this crystal.

The $\rho(T)$ for the CoAs-flux-grown crystal #3 is shown in Fig. 22(b), where $\rho_0 = 16.0 \mu\Omega \text{ cm}$ at $T = 1.8$ K and $\text{RRR} = 2.16$. The AFM transition is observed at $T_N = 40.0(9)$ K, as clearly shown in the plot of $d\rho(T)/dT$

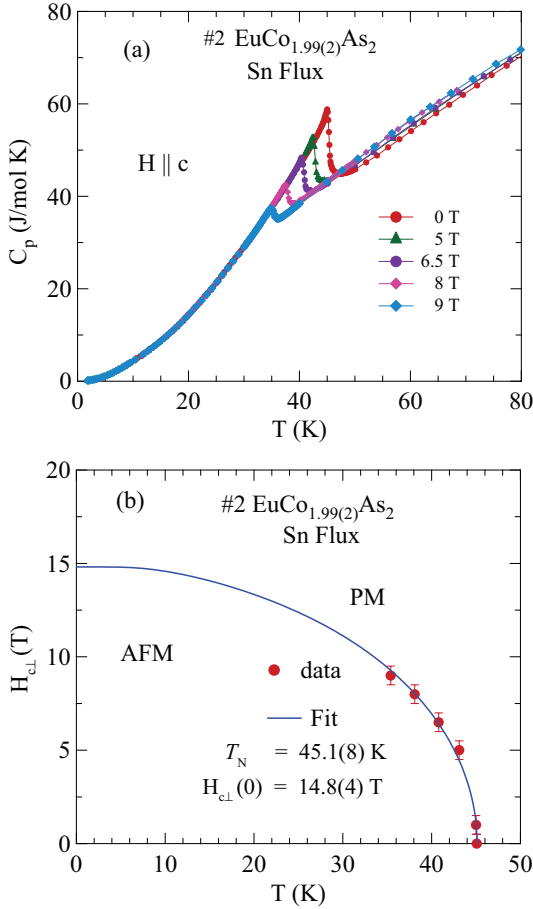


FIG. 19: (a) Heat capacity C_p versus temperature T of Sn-flux-grown crystal #2 $\text{EuCo}_{1.99(2)}\text{As}_2$ in various fields $H_{\perp} \equiv H \parallel c$ as listed. (b) Magnetic H_{\perp} - T phase diagram constructed from the $C_p(H, T)$ data in (a). The solid blue curve is a fit of the data points by Eq. (27a).

in Fig. 22(b) inset (1), again in agreement with T_N found from our $\chi(T)$ and $C_p(T)$ data for this crystal.

The low- T data below T_N was fitted well by the quadratic expression $\rho(T) = \rho_0 + AT^2$ corresponding to electron-electron scattering, as shown by the solid curve in Fig. 22(a) inset (2) for the Sn-flux-grown crystal and in Fig. 22(b) inset(2) for the CoAs-flux-grown crystal, where the fitting parameters are $A = 0.0022(1) \mu\Omega \text{ cm/K}^2$ for the Sn-flux-grown crystal, and $A = 0.0065(1) \mu\Omega \text{ cm/K}^2$ for the CoAs-flux-grown crystal.

The $\rho(T)$ above 50 K was fitted by the Bloch-Grüneisen (BG) model where the resistivity arises from electron-phonon scattering, given by [68]

$$\rho_{\text{BG}}(T) = \rho_0 + F \left(\frac{T}{\Theta_R} \right)^5 \int_0^{\Theta_R/T} \frac{x^5 dx}{(1 - e^{-x})(e^x - 1)}, \quad (29)$$

where F is a numerical constant that describes the T -independent interaction strength of the conduction electrons with the thermally excited acoustic phonons and

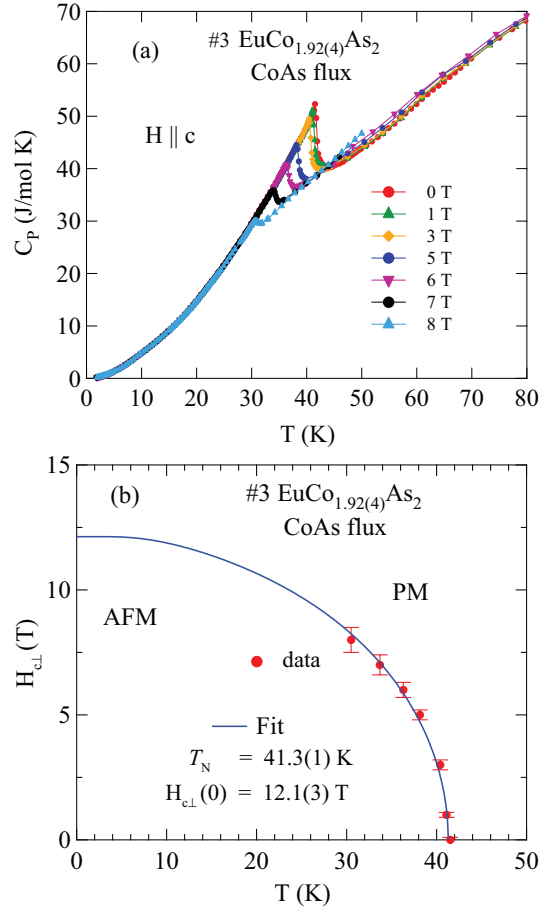


FIG. 20: Same as Fig. 19 except for CoAs-flux-grown crystal #3 $\text{EuCo}_{1.99(2)}\text{As}_2$ instead.

contains the ionic mass, Fermi velocity, and other parameters, $x = \frac{\hbar\omega}{2\pi k_B T}$, and Θ_R is the resistively-determined Debye temperature [68]. The representation for $\rho_{\text{BG}}(T)$ used here is an accurate analytic Padé approximant function of T/Θ_R [68]. The fits to the data between 70 and 320 K by Eq. (29) are shown as the yellow curves in the main panels of Figs. 22(a) and 22(b), and the fitted parameters are listed in Table VI.

On close examination, the BG model does not provide an optimum fit to the data in Fig. 22. A phenomenological model that can describe the negative curvature in $\rho(T)$ at high T is the so-called parallel-resistor model given by [69]

$$\frac{1}{\rho(T)} = \frac{1}{\rho_{\text{BG}}(T)} + \frac{1}{\rho_{\text{max}}}, \quad (30)$$

where ρ_{max} is the T -independent saturation resistivity which is also called the Ioffe-Regel limit [70], and $\rho_{\text{BG}}(T)$ is the Bloch-Grüneisen expression (29). We fitted the $\rho(T)$ data above T_N in the range $50 \text{ K} < T < 320 \text{ K}$ by Eq. (30) as shown by the red curves in Figs. 22(a) and 22(b). One sees that the data for both crystals are fitted well by the parallel-resistor model and the values

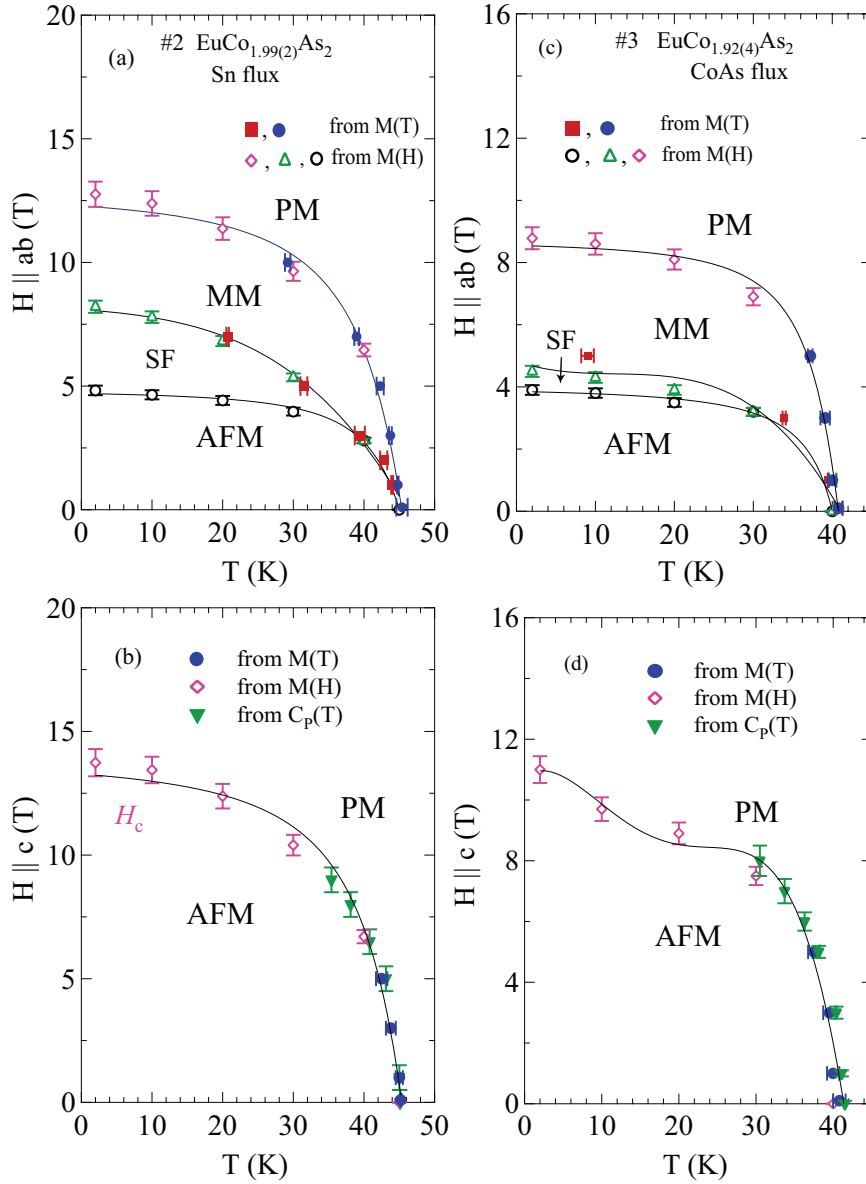


FIG. 21: The magnetic phase diagrams of (a,b) Sn-flux-grown crystal #2 $\text{EuCo}_{1.99(2)}\text{As}_2$ and (c,d) CoAs-flux-grown crystal #3 $\text{EuCo}_{1.92(4)}\text{As}_2$ for (a,c) $H \parallel ab$ and (b,d) $H \parallel c$.

of the parameters obtained from the fits are listed in Table VI. One sees from the table that the values of θ_R for the two crystals are closer to each other for the parallel-resistor fits compared to the BG fits by themselves and also the fit parameters have higher precision for the parallel-resistor fits.

The negative curvature in the resistivity at the higher temperature that is not fitted by the BG model may be either due to interband scattering or weak additional electron-electron scattering originating from the thermal population of higher-lying energy levels [71, 72]. A model that can describe the negative curvature $\rho(T)$ above the ordering temperature is the Bloch-Grüneisen-Mott

model, given by [73]

$$\rho_{\text{BGM}}(T) = \rho_{\text{BG}}(T) - \alpha T^3, \quad (31)$$

where $\rho_{\text{BG}}(T)$ is the Bloch-Grüneisen expression as shown by Eq.(29) and α is the s - d interband scattering coefficient (Mott coefficient). The fits of the model to the experimental data are shown by the solid green curves in Figs. 22(a) and 22(b). In this model, when the mean-free path is shorter than on the order of a few atomic spacings, the scattering cross section is no longer linear in T because under the influence of the lattice vibrations the s electrons may make transitions to the unoccupied or partially-filled d states. As a result, the resistance decreases with increasing temperature and shows negative curvature ($d^2\rho/dT^2 < 0$).

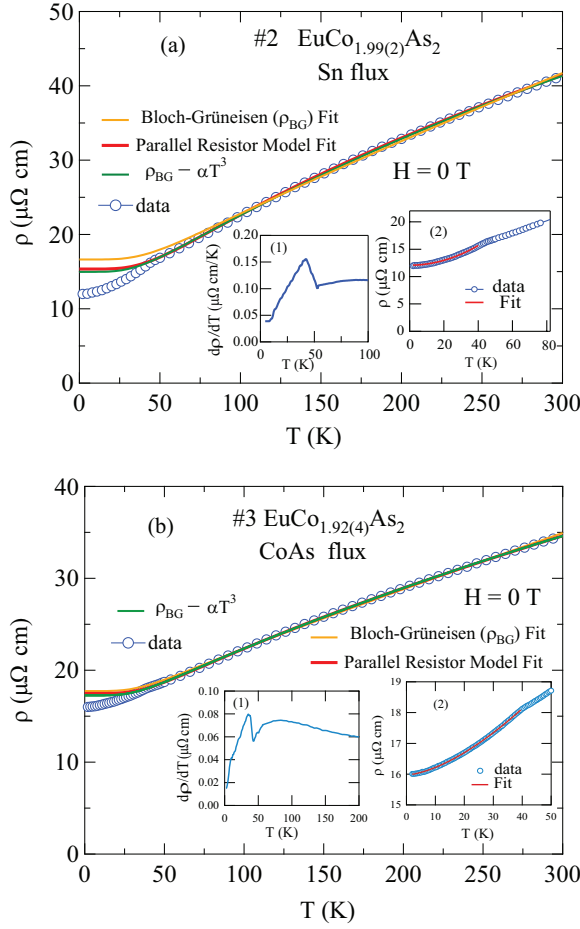


FIG. 22: In-plane electrical resistivity ρ versus temperature T of (a) Sn-flux-grown crystal #2 $\text{EuCo}_{1.99(2)}\text{As}_2$ and (b) CoAs-flux-grown crystal #3 $\text{EuCo}_{1.92(4)}\text{As}_2$ as a function of temperature T measured in zero magnetic field. Insets (1): Temperature derivatives $d\rho/dT$ versus T . Insets (2): Expanded plots of $\rho(T)$ at low temperatures. The straight red lines in insets (2) are fits by $\rho = \rho_0 + AT^2$ over the temperature interval $2 \text{ K} \leq T \leq 43 \text{ K}$. The fit parameters are listed in Table VI. The three fits are almost indistinguishable on the scale of the figure.

B. High-Field Resistivity

The $\rho(T)$ data at selected magnetic fields applied along the c -axis for the $\text{EuCo}_{2-y}\text{As}_2$ crystals grown from Sn flux (#2) and CoAs flux (#3) are shown in Figs. 23(a) and 24(a), respectively. For the Sn-flux-grown crystal, the $d\rho(T)/dT$ data in Fig. 23(a) show that the peak position at T_N shifts from 45.0(4) K at $H = 0$ to 35.2(5) K at $H = 8 \text{ T}$ and the transition broadens and smears out progressively with increasing field up to 8 T. For the CoAs-grown crystal, T_N shifts from 40.0(9) K to 25.5(3) K with increasing field up to 9 T. The field-dependent $\rho(H, T)$ data for CoAs-flux-grown and Sn-flux-grown crystals show different shapes below T_N .

The magnetoresistance (MR), defined as $\text{MR}(H, T) \equiv$

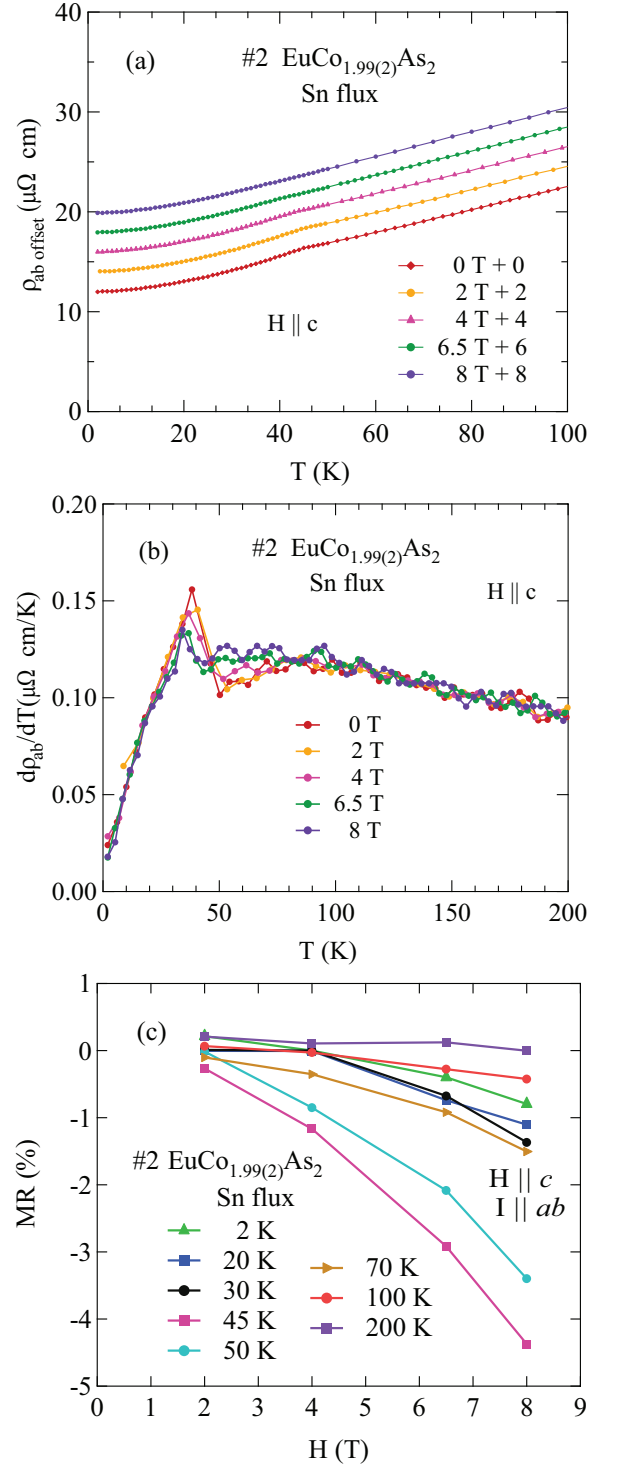


FIG. 23: (a) In-plane electrical resistivity ρ of Sn-flux-grown crystal #2 $\text{EuCo}_{1.99(2)}\text{As}_2$ as a function of temperature T measured in the indicated magnetic fields $H \parallel c$. For clarity, the data for successive fields are offset from each other by $2 \mu\Omega \text{ cm}$ as indicated. (b) Temperature derivative $d\rho/dT$ versus T obtained from the data in (a). (c) Magnetoresistance MR versus applied field at temperatures ranging from 2 to 20 K for current density $J \parallel ab$ and magnetic fields $H \parallel c$.

TABLE VI: The parameters obtained from Bloch-Grüneisen, Parallel Resistor, and sd -Scattering fits obtained using Eqs. (29), (30), and (31), respectively, to $\rho(T)$ data for $\text{EuCo}_{2-y}\text{As}_2$ single crystals in the temperature range $50 \text{ K} < T < 320 \text{ K}$.

| Crystal: | #2 $\text{EuCo}_{1.99(2)}\text{As}_2^a$ | #3 $\text{EuCo}_{1.92(4)}\text{As}_2^b$ |
|---|---|---|
| <u>Fit</u> | | |
| <u>Bloch-Grüneisen</u> | | |
| ρ_0 ($\mu\Omega \text{ cm}$) | 16(1) | 17.7(3) |
| F ($\mu\Omega \text{ cm}$) | 21(5) | 12(1) |
| Θ_R (K) | 257(6) | 213(3) |
| <u>Parallel-Resistor</u> | | |
| ρ_0 ($\mu\Omega \text{ cm}$) | 16.87(4) | 19.55(4) |
| ρ_{max} ($\mu\Omega \text{ cm}$) | 168.9(9) | 164(1) |
| F ($\mu\Omega \text{ cm}$) | 32.9(2) | 18.3(2) |
| Θ_R (K) | 260(2) | 231(1) |
| <u>sd-Scattering</u> | | |
| ρ_0 ($\mu\Omega \text{ cm}$) | 14.7(1) | 17.38(2) |
| F ($\mu\Omega \text{ cm}$) | 20.4(6) | 12.8(1) |
| Θ_R (K) | 213(6) | 211(2) |
| α ($10^{-8} \mu\Omega \text{ cm/K}^3$) | 10.8(1) | 5.14(8) |

^aGrown in Sn flux with H_2 -treated Co powder

^bGrown in CoAs flux with H_2 -treated Co powder

$100\%[\rho(H, T) - \rho(0, T)]/\rho(0, T)$, calculated from the $\rho(H)$ data are shown in Fig. 23(c) and Fig. 24(c). At 2 K, the MR of Sn-flux-grown crystal is negative and attains a maximum negative value of -0.79% at 8 T whereas for the CoAs-flux-grown crystal, the MR at 9 T is -6.6% at 2 K. The negative curvature in MR versus H is enhanced as T_N is approached, leading to a MR of a -4.4% for the Sn-flux-grown crystal at $H = 8 \text{ T}$ and $T_N = 45 \text{ K}$, and a MR of -7.6% for the CoAs-flux-grown crystal at $H = 9 \text{ T}$ and $T_N = 40 \text{ K}$. At higher temperatures $T > T_N$, the MR shows positive curvature at low fields, and becomes positive at 200 K.

In the AFM-ordered state, the exchange interactions tend to align the spins in a different way than an external magnetic field does. As T_N is approached from below, the average coupling of the exchange interactions with the conduction electrons is reduced. Hence the Eu spins become better aligned with the applied field. This results in a reduction of the spin-disorder scattering, leading to an enhanced negative MR as T_N is approached. However, increasing T also results in an increase in spin-disorder scattering due to spin randomization by the thermal energy. Eventually spin-disorder by thermal energy dominates spin alignment by the applied magnetic field, resulting in a positive MR as seen at 200 K [74].

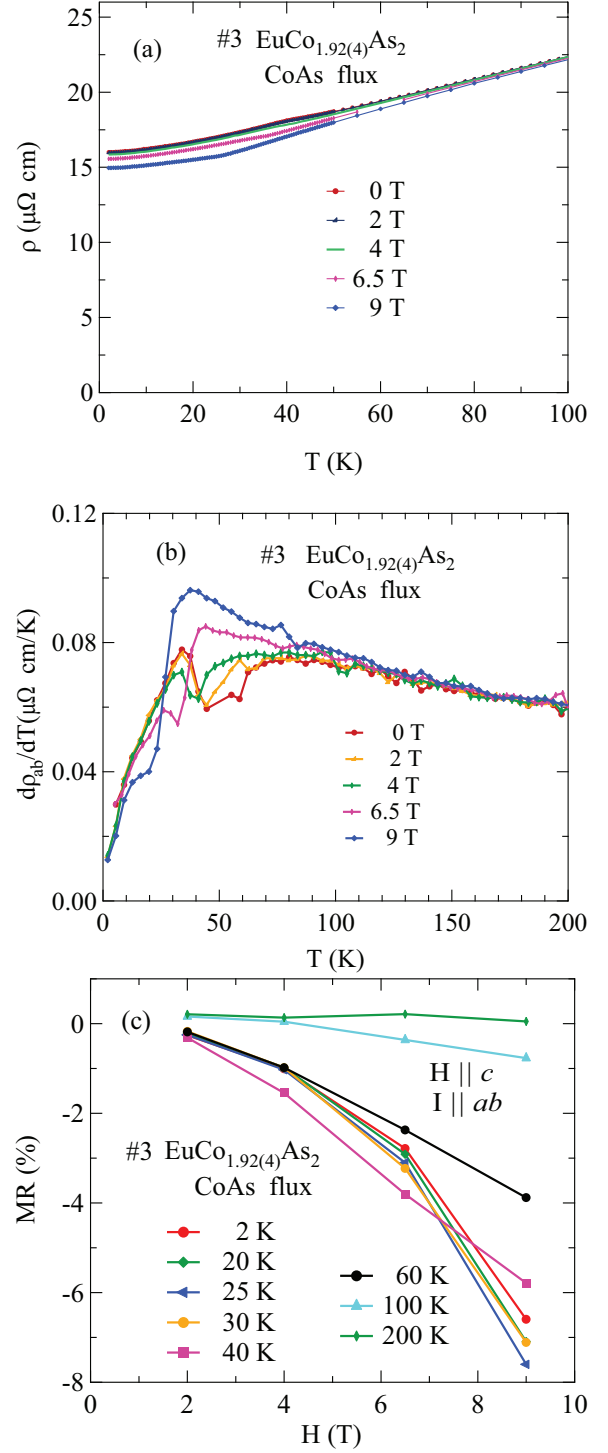


FIG. 24: Same as Fig. 23 but with CoAs-flux-grown single crystal #3 $\text{EuCo}_{1.92(4)}\text{As}_2$ instead.

VIII. ELECTRONIC STRUCTURE CALCULATIONS

In order to gain further insight on the enhanced Eu moments we performed electronic structure calculations. Our goals were (i) to check whether there is an enhanced

polarization that could justify the observed enhanced effective moment, (ii) if so, to find where it resides, and (iii) how the density of states relates to the measured specific heat.

We performed total energy, and band structure calculations employing the implementation of density functional theory in the code Dmol³ [75] within Materials Studio. This was done for the stoichiometric 122 system. Since we have permanent magnetic moments due to the $8S_{7/2}$ configuration of the Eu 4*f* electrons, we must do spin polarized calculations; otherwise DFT would wrongly split the 4*f* electrons equally over spin-up and spin-down states. We performed a calculation with all Eu spins pointing in the same direction, and another with alternating orientation in consecutive *ab* planes (from here on referred as configurations F and A, respectively). Although these are only two amongst the infinitely many configurations visited by the system in a paramagnetic state, such a comparison can give us information on how the relative orientation of the local spins can affect the polarization of the conduction band. This is motivated by the fact that EuCo_{2-y}As₂ is metallic and it is very likely that exchange interactions between the local moments and the conduction band play a role in the magnetic properties. In addition, the antiferromagnetic ground state should result in zero net polarization of the conduction electrons, while this does not have to be the case for other configurations.

Our calculations included all electrons (i.e., no pseudo-potential was used) in the scalar relativistic approximation. We employed the Perdew-Burke-Ernzerhof exchange correlation functional [76] in the generalized gradient approximation. The Kohn-Sham quasiparticle states were sampled over a **k**-space grid with $7 \times 7 \times 9$ points and the **k**-space integration for the total energy was done with the tetrahedron method [77]. Self-consistency tolerance was set to 2×10^{-6} Rydberg for the total energy per cell.

The band structures in both configurations are shown in Fig. 25. Projected density of states on atomic orbital type for configurations F and A are shown in Figs. 26 and 27, respectively. One can notice in Fig. 26 that the polarization induced by the local Eu moments resides in the *d* states, which are mainly coming from cobalt atoms. Following the tetrahedral coordination of Co by As; one can roughly divide the *d* orbitals into two sets, the *e_g* doublet and the *t_{2g}* triplet. The former is less affected by the As 4*p* states and appear less hybridized between -2.5 eV and -1 eV. The *t_{2g}* states mix more strongly with the As *p* states resulting in a bonding fraction between -4 eV and -3 eV (with dominant contribution from As *p* orbitals), and an antibonding component at and above the Fermi energy E_F (with dominant cobalt *d* contribution). While *d* states with different spin orientations are shifted with respect to each other at all energies in the F configuration, the *e_g* states have no net polarization as they appear fully occupied below E_F . The net polarization originates from the *t_{2g}* states around E_F . States with the

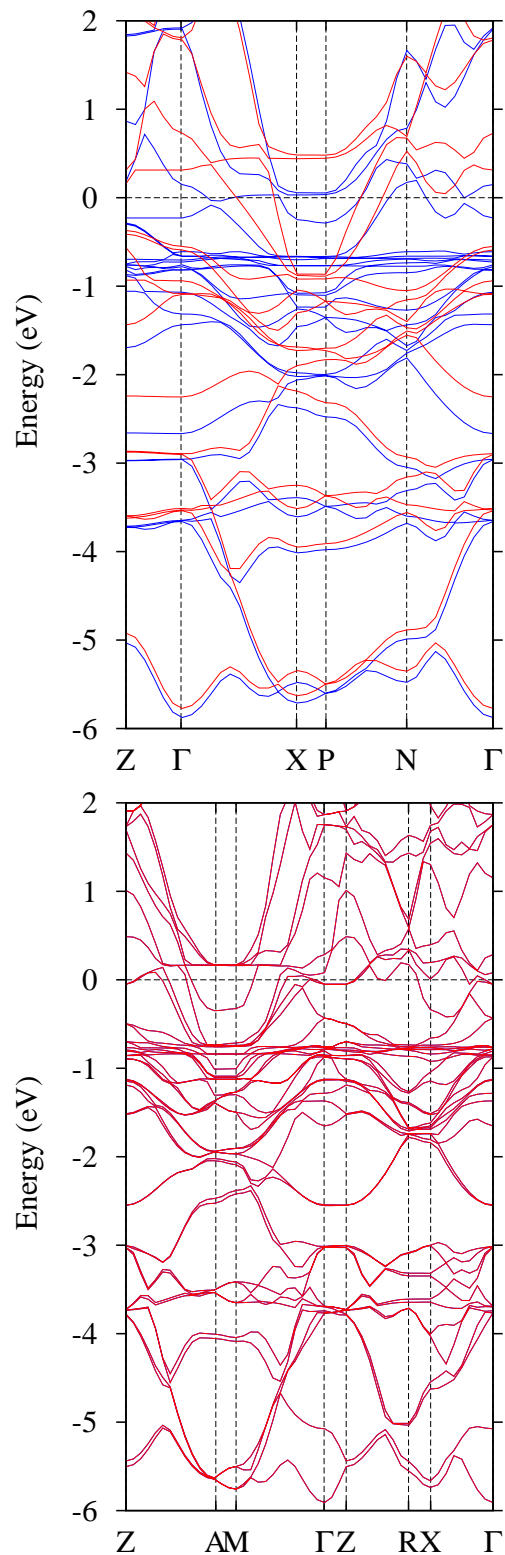


FIG. 25: Electronic band structure from DFT calculations for EuCo₂As₂ with Eu moments in configuration F (top) and A (bottom). Only states at energies above -6 eV (with respect to the Fermi energy E_F) are shown. These bands are mainly formed by As 4*p*, Co 3*d*, and the localized Eu 4*f* states which appear around -0.8 eV.

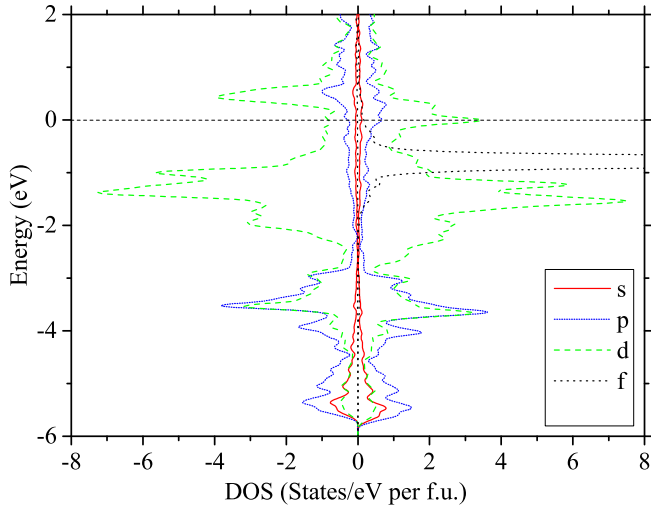


FIG. 26: Electronic density of states (DOS) from DFT calculations for EuCo_2As_2 with the Eu moments in configuration F. The projection of the s states is shown as the solid red curve, p as the short-dotted blue curve, d as the dashed green curve, and f as dotted-black curve.

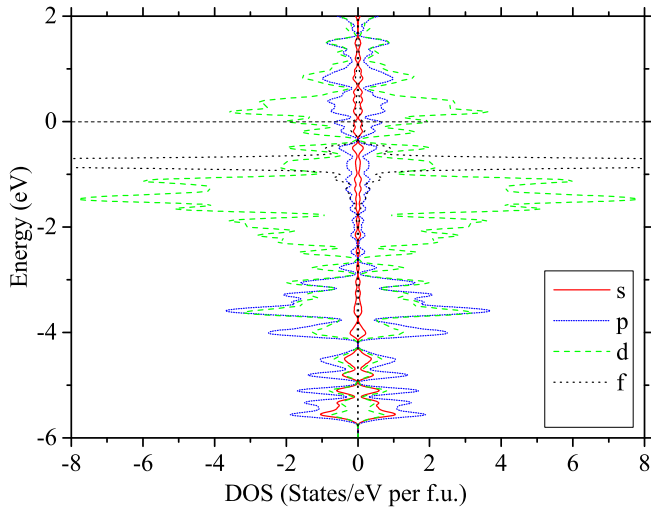


FIG. 27: Electronic density of states (DOS) from DFT calculations for EuCo_2As_2 with the Eu moments in configuration A. The projection of the s states is shown as the solid red curve, p as the short-dotted blue curve, d as the dashed green curve, and f as dotted-black curve.

same spin orientation as the Eu moments are stabilized (shifted down in energy) and those with the opposite orientation are shifted up (destabilized), resulting in a net enhanced moment per Eu atom.

In configuration F, the projection of the electronic states onto atomic centers gives $7/2$ spin for europium ions and 0.26 for the states belonging to cobalt. In configuration A, the total projected moment on the Eu sites remains as $7/2$ while the cobalt states display a negligible polarization of ± 0.01 . This is in agreement

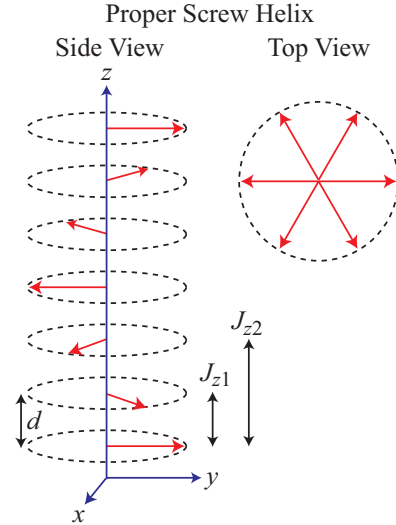


FIG. 28: Generic helix AFM structure [57]. Each arrow represents a layer of moments perpendicular to the z axis that are ferromagnetically aligned within the xy plane and with interlayer separation d . The wave vector \mathbf{k} of the helix is directed along the z axis. The magnetic moment turn angle between adjacent magnetic layers is kd . The exchange interactions J_{z1} and J_{z2} within the J_0 - J_{z1} - J_{z2} Heisenberg MFT model are indicated.

with the conclusion from neutron diffraction experiments that Co makes no contribution to the moments in the low-temperature ordered AFM phase. It is also consistent with the observation that in the paramagnetic state, the fluctuating moments have an enhanced value. As a very rough estimate, we can consider that having two Co per Eu, which are only polarized half of the time and fully correlated with the orientation of the Eu spins, the effective moment per Eu turns out to be $\mu_{\text{eff}} \sim 2\sqrt{(7/2 + 0.26) \times (7/2 + 0.26 + 1)} \approx 8.5$. This estimate is suggestively similar to the values obtained from the susceptibility fits.

The total electronic density of states at the Fermi level is predicted to have a very similar value of $D(E_F) \approx 5$ states/eV per f.u. for both F and A configurations. This value is comparable to the value of ≈ 6 states/eV f.u. obtained in Table V from the high-temperature fit of Eqs. (23) to $C_p(T)$. The experimentally-derived value of $D(E_F)$ is indeed expected to be larger than the band-structure value due to enhancement of the experimental value by the electron-phonon interaction.

IX. HEISENBERG EXCHANGE INTERACTIONS

We now estimate the intralayer and interlayer Heisenberg exchange interactions within the minimal J_0 - J_{z1} - J_{z2} MFT model for a helix in Fig. 28 [78], where J_0 is the sum of all Heisenberg exchange interactions of a representative spin to all other spins in the same spin layer

perpendicular to the helix (c) axis, J_{1z} is the sum of all interactions of the spin with spins in an adjacent layer along the helix axis, and J_{2z} is the sum of all interactions of the spin with spins in a second-nearest layer. Within this model kd , T_N and θ_p are related to these exchange interactions by [56, 57]

$$\cos(kd) = -\frac{J_{z1}}{4J_{z2}}, \quad (32a)$$

$$T_N = -\frac{S(S+1)}{3k_B} [J_0 + 2J_{z1} \cos(kd) + 2J_{z2} \cos(2kd)], \quad (32b)$$

$$\theta_p = -\frac{S(S+1)}{3k_B} (J_0 + 2J_{z1} + 2J_{z2}), \quad (32c)$$

where a positive (negative) J corresponds to an AFM (FM) interaction. The three exchange constants J_0 , J_{z1} and J_{z2} are obtained by solving Eqs. (32) using $S = 7/2$, $kd = 0.79\pi$, and the T_N and $\theta_p = \theta_{p\text{ave}}$ values in Table III, and the results are listed in Table VII.

The classical energy per spin in an ordered spin system in $H = 0$ with no anisotropy and containing identical crystallographically-equivalent spins is

$$E_i = \frac{1}{2} \sum_j J_{ij} \mathbf{S}(\mathbf{R}_i) \cdot \mathbf{S}(\mathbf{R}_j), \quad (33)$$

where the factor of 1/2 arises because the energy of an interacting spin pair is equally shared between the two spins in the pair, the sum is over the neighboring ordered spins $\mathbf{S}(\mathbf{R}_j)$ of the given central spin $\mathbf{S}(\mathbf{R}_i)$ and the J_{ij} are the Heisenberg exchange interactions between each respective spin pair. Here we only consider Bravais spin lattices where the position of each spin is a position of inversion symmetry of the spin lattice such as the body-centered-tetragonal (bct) spin lattice in Fig. 29. We further restrict our attention to coplanar AFMs in which the ordered moments in the ordered AFM state are aligned in the xy plane such as for the coplanar helix.

The expression for the classical ground-state energy per spin obtained from Eq. (33) is

$$E_i = \frac{S^2}{2} \sum_j J_{ij} \cos \phi_{ji}, \quad (34)$$

where $\cos \phi_{ji} = \hat{\mathbf{S}}(\mathbf{R}_i) \cdot \hat{\mathbf{S}}(\mathbf{R}_j)$ and ϕ_{ji} is the azimuthal angle within the xy plane between the ordered spins $\mathbf{S}(\mathbf{R}_j)$ and $\mathbf{S}(\mathbf{R}_i)$. Within the J_0 - J_{z1} - J_{z2} model one obtains

$$E_i = \frac{S^2}{2} [J_0 + 2J_{z1} \cos(kd) + 2J_{z2} \cos(2kd)], \quad (35)$$

where we take the ground-state turn angle to be $kd = 0.79\pi$ for all $\text{EuCo}_{2-y}\text{As}_2$ samples. Using $S = 7/2$ and the values of J_0 , J_{z1} and J_{z2} in Table VII, one obtains the classical ground-state energies per spin E_i listed in Table VII. The values are in the range -46 K to -52 K, with magnitudes that are similar to the Néel temperatures themselves as might have been expected.

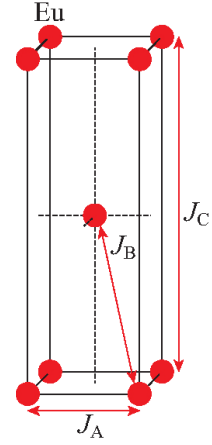


FIG. 29: Body-centered tetragonal Eu sublattice, where $c/a = 2.93$. The Heisenberg exchange interactions J_A , J_B and J_C are defined in the figure.

The bct Eu sublattice of EuCo_2As_2 is shown in Fig. 29, where the measured ratio $c/a = 2.93$ is to scale. Assuming that the exchange interactions J_A , J_B and J_C in the figure are the only ones present, in terms of the interactions in the J_0 - J_{z1} - J_{z2} model one has

$$J_0 = 4J_A, \quad J_{z1} = 4J_B, \quad J_{z2} = J_C. \quad (36)$$

Then using the values of J_0 , J_{z1} and J_{z2} in Table VII one obtains the J_A , J_B , and J_C values which are listed in Table VII.

X. SUMMARY

Investigations of the physical properties of $\text{EuCo}_{2-y}\text{As}_2$ crystals with the ThCr_2Si_2 structure that were grown in Sn and CoAs fluxes are reported. For most of our crystals, we find $\approx 5\%$ vacancies on the Co sites, similar to the value of 7% vacancies on the Co sites in $\text{CaCo}_{2-y}\text{As}_2$ [29, 30].

In-plane electrical resistivity $\rho(T)$ measurements indicate metallic behavior of the two crystals studied, with a kink in $\rho(T)$ at the respective T_N . High-field $\rho(T)$ data with $H \parallel c$ reveal negative magnetoresistance, reaching $\approx -5\%$ at $T = 2$ K and $H = 9$ T.

$\text{EuCo}_{2-y}\text{As}_2$ contains Eu^{+2} ions with expected spin $S = 7/2$ and $g = 2$, which exhibit AFM ordering at ≈ 45 K for the Sn-flux-grown crystals and ≈ 41 K for the CoAs-flux-grown crystals. We obtained good fits using molecular-field theory (MFT) to the low-field ab -plane magnetic susceptibility of the helical AFM structure below T_N with the Eu moments aligned in the ab plane. Zero-field heat capacity C_p measurements were carried out and the magnetic contribution $C_{\text{mag}}(T)$ was extracted. The $C_{\text{mag}}(T)$ data below T_N were fitted reasonably well by MFT. The $C_{\text{mag}}(T)$ above T_N is nonzero, indicating the presence of dynamic short-range AFM ordering above T_N . Thus the molar magnetic entropy S_{mag}

TABLE VII: Exchange constants in the J_0 - J_{z1} - J_{z2} model obtained from Eqs. (32) and the corresponding classical ground-state energies per spin E_i calculated from Eq. (35). The exchange interactions between Eu spins J_A , J_B and J_C obtained using Eq. (36) are also listed. Negative J values are FM and positive values are AFM.

| Compound | J_0/k_B (K) | J_{z1}/k_B (K) | J_{z2}/k_B (K) | E_i/k_B (K) | J_A/k_B (K) | J_B/k_B (K) | J_C/k_B |
|---|------------------|---------------------|---------------------|------------------|------------------|------------------|-----------|
| #1 $\text{EuCo}_{1.90(1)}\text{As}_2^a$ | -6.85 | 1.222 | 0.387 | -50.1 | -1.712 | 0.306 | 0.387 |
| #2 $\text{EuCo}_{1.99(2)}\text{As}_2^b$ | -6.84 | 1.200 | 0.380 | -49.9 | -1.711 | 0.300 | 0.380 |
| #3 $\text{EuCo}_{1.92(4)}\text{As}_2^c$ | -6.58 | 0.836 | 0.265 | -45.9 | -1.645 | 0.209 | 0.265 |
| #4 $\text{EuCo}_{1.90(2)}\text{As}_2^d$ | -6.54 | 0.853 | 0.270 | -45.7 | -1.635 | 0.213 | 0.270 |
| #5 $\text{EuCo}_{1.92(1)}\text{As}_2^d$ | -6.60 | 0.755 | 0.239 | -47.0 | -1.651 | 0.189 | 0.239 |
| $\text{EuCo}_2\text{As}_2^d$ [47] | -6.87 | 0.606 | 0.192 | -46.1 | -1.718 | 0.151 | 0.192 |
| $\text{EuCo}_2\text{As}_2^e$ [44] | -6.77 | 1.533 | 0.485 | -51.7 | -1.693 | 0.383 | 0.485 |

^aGrown in Sn flux

^bGrown in Sn flux with H₂-treated Co powder

^cGrown in CoAs flux with H₂-treated Co powder

^dGrown in CoAs flux

^eGrown in Bi flux

at T_N is only about 90% of the completely disordered value $R \ln 8$, the remainder being recovered by about 70 K.

The high-field magnetization in the ab plane below T_N exhibits a spin-flop-like transition followed by a second-order metamagnetic transition to an unknown AFM structure and then a second-order AFM to paramagnetic (PM) transition, whereas high-field c -axis measurements reveal a second-order transition of unknown nature in addition to the expected second-order canted-AFM to PM transition. High-field $C_p(T)$ measurements with $H \parallel c$ only reveal the AFM to PM transition, where the T_N and the heat capacity jump at T_N both decrease with increasing H . Phase diagrams in the $H \parallel ab$ and $H \parallel c$ versus T planes were constructed from the high-field magnetization and heat capacity results.

A primary goal of the present work was to investigate a possible enhancement of the Eu magnetic moment for crystals of $\text{EuCo}_{2-y}\text{As}_2$ prepared under different conditions. Shown in Table VIII is a summary of the effective moments μ_{eff} obtained from modified Curie-Weiss law fits in the paramagnetic state at $T > T_N$ for five of the crystals studied here and the corresponding saturation moments μ_{sat} obtained from high-field $M(H)$ isotherms at $T = 2$ K of $\text{EuCo}_{2-y}\text{As}_2$ from Tables III and IV, respectively. These two moments are given in general for a spin with no contribution of orbital moments by

$$\mu_{\text{eff}} = g\sqrt{S(S+1)}\mu_B, \quad (37a)$$

$$\mu_{\text{sat}} = gS\mu_B. \quad (37b)$$

For spin-only Eu^{+2} , one expects $S = 7/2$ and $g \approx 2$, yielding

$$\mu_{\text{eff}0} = 7.94\mu_B/\text{Eu}, \quad (38a)$$

$$\mu_{\text{sat}0} = 7.00\mu_B/\text{Eu} \quad (38b)$$

Comparing these values with those in Table VIII shows that both Sn-flux-grown and CoAs-flux-grown crystals

show significant enhancements of μ_{eff} and/or μ_{sat} . Also shown in the table are the relative enhancements of the observed moments with respect to the expected moments as expressed by $\Delta\mu/\mu_0 \equiv (\mu_{\text{obs}} - \mu_0)/\mu_0$. One sees that the effective moment μ_{eff} values are all enhanced by 6.7% to 9.1% with respect to the unenhanced value. The saturation moments μ_{sat} also exhibit enhancements, but the enhancement is more variable, from 0.4% to 8.4%.

Shown in Fig. 30(a) is a plot of T_N versus the tetragonal c/a ratio obtained using the data in Tables I and VIII. One sees an approximately linear positive correlation between T_N and c/a . On the other hand, the correlations between μ_{eff} and μ_{sat} versus c/a show no clear correlation.

If one does not include a T -independent term χ_0 when fitting the paramagnetic-state data by the Curie-Weiss law, negative curvature is usually observed in the $\chi^{-1}(T)$ plots which according to Fig. 5 would then be attributed to an effective moment that increases with decreasing temperature. We calculated an approximate value of χ_0 which is negative but with a magnitude far smaller than the diamagnetic fitted values for our crystals. This suggests that indeed the Curie constant and hence effective moment may be temperature-dependent, increasing with decreasing temperature.

Table VIII also contains literature data for μ_{eff} and μ_{sat} for several other 122-type compounds containing Eu^{+2} spins. One sees that the respective values for all these compounds are less than the expected value. This divergence between the values of the Eu moments in $\text{EuCo}_{2-y}\text{As}_2$ and those of the other compounds starkly illustrates the anomalous enhancement of the Eu moments in $\text{EuCo}_{2-y}\text{As}_2$.

From Eqs. (37), enhancement of the Eu moment could arise from enhancement of g , of S , or both. Such an enhancement occurs in ferromagnetic Gd metal containing Gd^{+3} ions with $S = 7/2$, where the saturation moment

TABLE VIII: Effective moment μ_{eff} and saturation moment μ_{sat} at $T = 2$ K of $\text{EuCo}_{2-y}\text{As}_2$ obtained from Tables III and IV. The fourth and sixth columns show the deviations of these quantities from the theoretical values in Eqs. (38). Literature data for other compounds are also shown.

| Crystal Designation | Field Direction | μ_{eff} (μ_{B}/Eu) | $\frac{\Delta\mu_{\text{eff}}}{\mu_{\text{eff0}}}$ (%) | μ_{sat} (μ_{B}/Eu) | $\frac{\Delta\mu_{\text{sat}}}{\mu_{\text{sat0}}}$ (%) |
|--|--------------------|--|---|--|---|
| #1 $\text{EuCo}_{1.90(1)}\text{As}_2^a$ | $H \parallel ab$ | 8.48 | 6.8 | 7.15 | 2.1 |
| | $H \parallel c$ | 8.47 | 6.7 | 7.05 | 0.7 |
| #2 $\text{EuCo}_{1.99(2)}\text{As}_2^b$ | $H \parallel ab$ | 8.59 | 8.2 | 7.03 | 0.4 |
| | $H \parallel c$ | 8.66 | 9.1 | 7.05 | 0.7 |
| #3 $\text{EuCo}_{1.92(4)}\text{As}_2^c$ | $H \parallel ab$ | 8.59 | 8.1 | 7.59 | 8.4 |
| | $H \parallel c$ | 8.49 | 6.9 | 7.57 | 8.1 |
| #4 $\text{EuCo}_{1.90(2)}\text{As}_2^d$ | $H \parallel ab$ | 8.51 | 7.2 | 7.34 | 4.9 |
| | $H \parallel c$ | 8.50 | 7.1 | 7.19 | 2.7 |
| #5 $\text{EuCo}_{1.90(2)}\text{As}_2^d$ | $H \parallel ab$ | 8.56 | 7.8 | 7.50 | 7.1 |
| | $H \parallel c$ | 8.71 | 9.7 | 7.58 | 8.3 |
| EuCo_2As_2 [44] | | | | 7.26(8) ^f | 3.7 |
| EuCo_2P_2 [40, 43] | $H \parallel ab$ | 7.83(1) | -1.4 | 6.9(1) ^g | -1.4 |
| | $H \parallel c$ | 7.84(1) | -1.3 | | |
| EuFe_2As_2 [79] | | | | 6.8(3) ^g | -2.9 |
| $\text{EuPd}_2\text{Sb}_2^e$ [80] | | 7.61(2) | -4.2 | | |
| EuCu_2As_2 [81] | $H \parallel ab$ | 7.72(1) | -2.8 | 6.66 | -4.9 |
| | $H \parallel c$ | 7.82(1) | -1.5 | 6.77 | -3.3 |
| $\text{EuCu}_{1.82}\text{Sb}_2^e$ [81, 82] | $H \parallel ab$ | 7.70(1) | -3.0 | 6.76 ^h | -3.4 |
| | $H \parallel c$ | 7.77(1) | -2.1 | 6.95 | -0.7 |

^aGrown in Sn flux

^bGrown in Sn flux with H₂-treated Co powder

^cGrown in CoAs flux with H₂-treated Co powder

^dGrown in CoAs flux

^ePrimitive-tetragonal CaBe_2Ge_2 structure with space group $P4/nmm$

^fCrystal grown in Bi flux; no Co vacancies detected; neutron diffraction measurement

^gFrom neutron-diffraction measurements [40]

^hNeutron-diffraction measurements [82] give an ordered moment of 7.08(15) μ_{B}/Eu

at 4.2 K is 7.55(2) μ_{B}/Gd [83]. This enhancement above the expected value 7 μ_{B}/Gd was found from electronic structure calculations to arise from polarization of the conduction d -band electrons by the Gd spins [84]. The enhancement is similar to the maximum enhancements of the moment of isoelectronic Eu^{+2} with $S = 7/2$ in Table VIII. It has been inferred from neutron diffraction studies [46] that the Co atoms do not contribute to the ordered moment of $\text{EuCo}_{2-y}\text{As}_2$ below T_{N} . It therefore seems likely that the effective spin value is increased by polarization of the conduction carrier spins by the ordered Eu spins. This expectation is indeed confirmed by our electronic structure calculations.

Acknowledgments

We thank Shalabh Gupta for the H₂ treatment of our Co powder starting material, George Lindemann for his help during the early stages of this work, and Michael Shatruk for sending us his published $\chi(T)$ data for an EuCo_2As_2 crystal [44]. The research at Ames was supported by the U.S. Department of Energy, Office of Basic Energy Sciences, Division of Materials Sciences and Engineering. Ames Laboratory is operated for the U.S. Department of Energy by Iowa State University under Contract No. DE-AC02-07CH11358.

[1] D. C. Johnston, The puzzle of high temperature superconductivity in layered iron pnictides and chalcogenides,

Adv. Phys. **59**, 803 (2010).

[2] G. R. Stewart, Superconductivity in iron compounds,

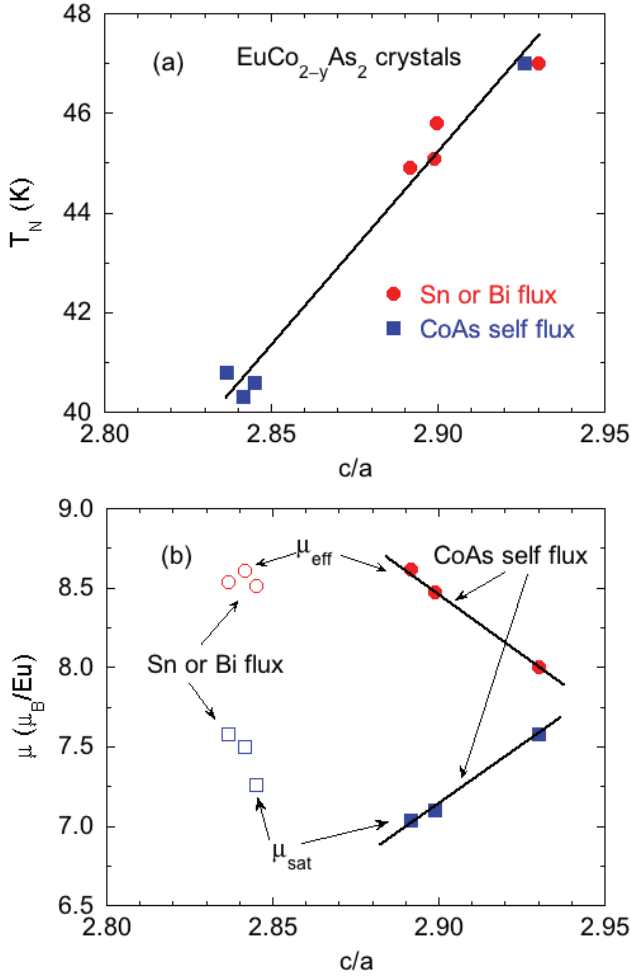


FIG. 30: (a) Néel temperature T_N versus crystallographic c/a ratio for $\text{EuCo}_{2-y}\text{As}_2$ crystals grown with Sn or Bi flux or with CoAs self-flux. (b) Effective moment μ_{eff} and saturation moment μ_{sat} versus c/a . Data from Refs. [44] and [46] are included. The lines in (a) and (b) are guides to the eye.

Rev. Mod. Phys. **83**, 1589 (2011).

[3] D. J. Scalapino, A common thread: The pairing interaction for unconventional superconductors, Rev. Mod. Phys. **84**, 1383 (2012).

[4] E. Dagotto, The unexpected properties of alkali metal iron selenide superconductors, Rev. Mod. Phys. **85**, 849 (2013).

[5] R. M. Fernandes, A. V. Chubukov, and J. Schmalian, What drives nematic order in iron-based superconductors? Nat. Phys. **10**, 97 (2014).

[6] H. Hosono and K. Kuroki Iron-based superconductors: Current status of materials and pairing mechanism, Physica C **514**, 399 (2015).

[7] P. Dai, Antiferromagnetic order and spin dynamics in iron-based superconductors, Rev. Mod. Phys. **87**, 855 (2015).

[8] D. S. Inosov, Spin fluctuations in iron pnictides and chalcogenides: From antiferromagnetism to superconductivity, Compt. Rend. Phys. **17**, 60 (2016).

[9] Q. Si, R. Yu, and E. Abrahams, High-temperature su-

perconductivity in iron pnictides and chalcogenides, Nat. Rev. Mater. **1**, 1 (2016).

[10] J. An, A. S. Sefat, D. J. Singh, and M.-H. Du, Electronic structure and magnetism in BaMn_2As_2 and BaMn_2Sb_2 , Phys. Rev. B **79**, 075120 (2009).

[11] Y. Singh, A. Ellern, and D. C. Johnston, Magnetic, transport, and thermal properties of single crystals of the layered arsenide BaMn_2As_2 , Phys. Rev. B **79**, 094519 (2009).

[12] Y. Singh, M. A. Green, Q. Huang, A. Kreyssig, R. J. McQueeney, D. C. Johnston, and A. I. Goldman., Magnetic order in BaMn_2As_2 from neutron diffraction measurements, Phys. Rev. B **80**, 100403(R) (2009).

[13] D. C. Johnston, R. J. McQueeney, B. Lake, A. Honecker, M. E. Zhitomirsky, R. Nath, Y. Furukawa, V. P. Antropov, and Y. Singh, Magnetic Exchange Interactions in BaMn_2As_2 : A Case Study of the J_1 - J_2 - J_c Heisenberg Model, Phys. Rev. B **84**, 094445 (2011).

[14] A. Antal, T. Knoblauch, Y. Singh, P. Gegenwart, D. Wu, and M. Dressel, Optical properties of the iron-pnictide analog BaMn_2As_2 , Phys. Rev. B **86**, 014506 (2012).

[15] S. Calder, B. Sagarov, H. B. Cao, J. L. Niedziela, M. D. Lumsden, A. S. Sefat, and A. D. Christianson, Magnetic structure and spin excitations in BaMn_2Bi_2 . Phys. Rev. B **89**, 064417 (2014).

[16] W.-L. Zhang, P. Richard, A. van Roekeghem, S.-M. Nie, N. Xu, P. Zhang, H. Miao, S.-F. Wu, J.-X. Yin, B. B. Fu, L.-Y. Kong, T. Qian, Z.-J. Wang, Z. Fang, A. S. Sefat, S. Biermann, and H. Ding. Angle-resolved photoemission observation of Mn-pnictide hybridization and negligible band structure renormalization in BaMn_2As_2 and BaMn_2Sb_2 . Phys. Rev. B **94** 155155 (2016).

[17] N. S. Sangeetha, A. Pandey, Z. A. Benson, and D. C. Johnston, Strong magnetic correlations to 900 K in single crystals of the trigonal antiferromagnetic insulators SrMn_2As_2 and CaMn_2As_2 , Phys. Rev. B **94**, 094417 (2016).

[18] P. Das, N. S. Sangeetha, A. Pandey, Z. A. Benson, T. W. Heitmann, D. C. Johnston, A. I. Goldman, and A. Kreyssig, Collinear antiferromagnetism in trigonal SrMn_2As_2 revealed by single-crystal neutron diffraction, J. Phys.: Condens. Matter **29**, 035802 (2017).

[19] N. S. Sangeetha, V. Smetana, A.-V. Mudring, and D. C. Johnston, Antiferromagnetism in semiconducting SrMn_2Sb_2 and BaMn_2Sb_2 single crystals, Phys. Rev. B **97**, 014402 (2018).

[20] D. J. Singh, A. S. Sefat, M. A. McGuire, B. C. Sales, D. Mandrus, L. H. VanBebber, and V. Keppens, Itinerant antiferromagnetism in BaCr_2As_2 : Experimental characterization and electronic structure calculations, Phys. Rev. B **79**, 094429 (2009).

[21] K. A. Filsinger, W. Schnelle, P. Adler, G. H. Fecher, M. Reehuis, A. Hoser, J.-U. Hoffmann, P. Werner, M. Greenblatt, and C. Felser, Antiferromagnetic structure and electronic properties of BaCr_2As_2 and BaCrFeAs_2 , Phys. Rev. B **95**, 184414 (2017).

[22] J. Nayak, K. Filsinger, G. H. Fecher, S. Chadov, J. Minar, E. E. D. Rienks, B. Büchner, J. Fink, and C. Felser, Observation of a remarkable reduction of correlation effects in BaCr_2As_2 by ARPES. arXiv:1701.06108.

[23] P. Richard, A. van Roekeghem, B. Q. Lv, T. Qian, T.K. Kim, M. Hoesch, J.-P. Hu, A. S. Sefat, S. Biermann, and H. Ding, Is BaCr_2As_2 symmetrical to BaFe_2As_2 with respect to half $3d$ shell filling? Phys. Rev. B **95**, 184516

- (2017).
- [24] U. B. Paramanik, R. Prasad, C. Geibel, and Z. Hossain, Itinerant and local-moment magnetism in EuCr_2As_2 single crystals, *Phys. Rev. B* **89**, 144423 (2014).
- [25] S. Nandi, Y. Xiao, N. Qureshi, U. B. Paramanik, W. T. Jin, Y. Su, B. Ouladdiaf, Z. Hossain, and Th. Brückel, Magnetic structures of the Eu and Cr moments in EuCr_2As_2 : Neutron diffraction study, *Phys. Rev. B* **94**, 094411 (2016).
- [26] M. Pfisterer and G. Nagorsen, On the Structure of Ternary Arsenides, *Z. Naturforsch.* **35b**, 703 (1980).
- [27] M. Pfisterer and G. Nagorsen, Bonding and Magnetic Properties in Ternary Arsenides ET_2As_2 , *Z. Naturforsch.* **38b**, 811 (1983).
- [28] For a discussion of the magnetic ordering behaviors of cT versus ucT AM_2X_2 compounds with $A = \text{Ca, Sr, Ba}$, $M = \text{Cr, Mn, Fe, Co, Ni}$, and $X = \text{P, As}$, see Sec. VIII of V. K. Anand, P. Kanchana Perera, A. Pandey, R. J. Goetsch, A. Kreyssig, and D. C. Johnston, Crystal growth and physical properties of SrCu_2As_2 , SrCu_2Sb_2 , and BaCu_2Sb_2 , *Phys. Rev. B* **85**, 214523 (2012).
- [29] V. K. Anand, R. S. Dhaka, Y. Lee, B. N. Harmon, A. Kaminski, and D. C. Johnston, Physical Properties of Metallic Antiferromagnetic $\text{CaCo}_{1.86}\text{As}_2$ Single Crystals, *Phys. Rev. B* **89**, 214409 (2014).
- [30] D. G. Quirinale, V. K. Anand, M. G. Kim, A. Pandey, A. Huq, P. W. Stephens, T. W. Heitmann, A. Kreyssig, R. J. McQueeney, D. C. Johnston, and A. I. Goldman, Crystal and magnetic structure of $\text{CaCo}_{1.86}\text{As}_2$ studied by x-ray and neutron diffraction, *Phys. Rev. B* **88**, 174420 (2013).
- [31] A. Pandey, D. G. Quirinale, W. Jayasekara, A. Sapkota, M. G. Kim, R. S. Dhaka, Y. Lee, T. W. Heitmann, P. W. Stephens, V. Oglolichiev, A. Kreyssig, R. J. McQueeney, A. I. Goldman, A. Kaminski, B. N. Harmon, Y. Furukawa, and D. C. Johnston, Crystallographic, electronic, thermal, and magnetic properties of single-crystal SrCo_2As_2 , *Phys. Rev. B* **88**, 014526 (2013).
- [32] V. K. Anand, D. G. Quirinale, Y. Lee, B. N. Harmon, Y. Furukawa, V. V. Ogloblichev, A. Huq, D. L. Abernathy, P. W. Stephens, R. J. McQueeney, A. Kreyssig, A. I. Goldman, and D. C. Johnston, Crystallography and physical properties of BaCo_2As_2 , $\text{Ba}_{0.94}\text{K}_{0.06}\text{Co}_2\text{As}_2$ and $\text{Ba}_{0.78}\text{K}_{0.22}\text{Co}_2\text{As}_2$, *Phys. Rev. B* **90**, 064517 (2014).
- [33] W. T. Jayasekara, U. S. Kaluarachchi, B. G. Ueland, A. Pandey, Y. B. Lee, V. Taufour, A. Sapkota, K. Kothapalli, N. S. Sangeetha, G. Fabbris, L. S. I. Veiga, Y. Feng, A. M. dos Santos, S. L. Bud'ko, B. N. Harmon, P. C. Canfield, D. C. Johnston, A. Kreyssig, and A. I. Goldman, Pressure-induced collapsed-tetragonal phase in SrCo_2As_2 , *Phys. Rev. B* **92**, 224103 (2015).
- [34] P. Wiecki, V. Ogloblichev, A. Pandey, D. C. Johnston, and Y. Furukawa, Coexistence of antiferromagnetic and ferromagnetic spin correlations in SrCo_2As_2 revealed by ^{59}Co and ^{75}As NMR, *Phys. Rev. B* **91**, 220406(R) (2015).
- [35] S. Jia, P. Jiramongkolchai, M. R. Suchomel, B. H. Toby, J. G. Checkelsky, N. P. Ong, and R. J. Cava, Ferromagnetic quantum critical point induced by dimer-breaking in $\text{SrCo}_2(\text{Ge}_{1-x}\text{P}_x)_2$, *Nature* **7**, 207 (2011).
- [36] T. Yildirim, Strong Coupling of the Fe-Spin State and the As-As Hybridization in Iron-Pnictide Superconductors from First-Principle Calculations, *Phys. Rev. Lett.* **102**, 037003 (2009).
- [37] T. Yildirim, Frustrated magnetic interactions, giant magnetoelastic coupling, and magnetic phonons in iron-pnictides, *Physica C* **469**, 425 (2009).
- [38] M. Reehuis, W. Jeitschko, G. Kotzyba, B. Zimmer, and X. Hu, Antiferromagnetic order in the ThCr_2Si_2 type phosphides CaCo_2P_2 and CeCo_2P_2 , *J. Alloys Compds.* **266**, 54 (1998).
- [39] E. Mörsen, B. D. Mosel, W. Müller-Warmuth, M. Reehuis, and W. Jeitschko, Mössbauer and Magnetic Susceptibility Investigations of Strontium, Lanthanum and Europium Transition Metal Phosphides with ThCr_2Si_2 Type Structure, *J. Phys. Chem. Solids* **49**, 785 (1988).
- [40] M. Reehuis, W. Jeitschko, M. H. Möller, and P. J. Brown, A Neutron Diffraction Study of the Magnetic Structure of EuCo_2P_2 , *J. Phys. Chem. Solids* **53**, 687 (1992).
- [41] C. Huhnt, W. Schlabitz, A. Wurth, A. Mewis, and M. Reehuis, First-order phase transitions in EuCo_2P_2 and SrNi_2P_2 , *Phys. Rev. B* **56**, 13796 (1997).
- [42] M. Chefki, M. M. Abd-Elmeguid, H. Micklitz, C. Huhnt, W. Schlabitz, M. Reehuis, and W. Jeitschko, Pressure-Induced Transition of the Sublattice Magnetization in EuCo_2P_2 : Change from Local Moment $\text{Eu}(4f)$ to Itinerant $\text{Co}(3d)$ Magnetism, *Phys. Rev. Lett.* **80**, 802 (1998).
- [43] N. S. Sangeetha, E. Cuervo-Reyes, A. Pandey, and D. C. Johnston, EuCo_2P_2 : A model molecular-field helical Heisenberg antiferromagnet, *Phys. Rev. B* **94**, 014422 (2016).
- [44] X. Tan, G. Fabbris, D. Haskel, A. A. Yaroslavl'tsev, H. Cao, C. M. Thompson, K. Kovnir, A. P. Menushenkov, R. V. Chernikov, V. O. Garlea, and M. Shatruk, A Transition from Localized to Strongly Correlated Electron Behavior and Mixed Valence Driven by Physical or Chemical Pressure in ACo_2As_2 ($A = \text{Eu}$ and Ca), *J. Am. Chem. Soc.* **138**, 2724 (2016).
- [45] R. Marchand and W. Jeitschko, Ternary Lanthanoid-Transition Metal Pnictides with ThCr_2Si_2 -Type Structure, *J. Solid State Chem.* **24**, 351 (1978).
- [46] H. Raffius, E. Mörsen, B. D. Mosel, W. Müller-warmuth, W. Jeitschko, L. Terbüchte, and T. Vomhof, Magnetic Properties Of Ternary Lanthanoid Transition Metal Arsenides Studied by Mössbauer and Susceptibility Measurements, *J. Phys. Chem. Solids* **54**, 135 (1993).
- [47] J. Ballinger, L. E. Wenger, Y. K. Vohra, and A. S. Sefat, Magnetic Properties of Single Crystal EuCo_2As_2 , *J. Appl. Phys.* **111**, 07E106 (2012).
- [48] M. Bishop, W. Uhoja, G. Tsoi, Y. K. Vohra, A. S. Sefat, and B. C. Sales, Formation of Collapsed Tetragonal Phase in EuCo_2As_2 , *J. Phys.: Condens. Matter* **22**, 425701 (2010).
- [49] Y. Fukai, S. Yokota, and J.-I. Yanagawa, The phase diagram and superabundant vacancy formation in Co-H alloys, *J. Alloys. Compd.* **407**, 16 (2006).
- [50] APEX3, Bruker AXS Inc., Madison, Wisconsin, USA, 2015.
- [51] SAINT, Bruker AXS Inc., Madison, Wisconsin, USA, 2015.
- [52] L. Krause, R. Herbst-Irmer, G. M. Sheldrick, and D. J. Stalke, Comparison of silver and molybdenum microfocus X-ray sources for single-crystal structure determination, *Appl. Crystallogr.* **48**, 3 (2015).
- [53] G. M. Sheldrick, SHELTX – Integrated space-group and crystal-structure determination, *Acta Crystallogr. A* **71**, 3 (2015).
- [54] G. M. Sheldrick, Crystal structure refinement with SHELXL, *Acta Crystallogr. C* **71**, 3 (2015).

- [55] M. E. Fisher, Relation between the Specific Heat and Susceptibility of an Antiferromagnet, *Phil. Mag.* **7**, 1731 (1962).
- [56] D. C. Johnston, Unified molecular field theory for collinear and noncollinear Heisenberg antiferromagnets, *Phys. Rev. B* **91**, 064427 (2015).
- [57] D. C. Johnston, Magnetic Susceptibility of Collinear and Noncollinear Heisenberg Antiferromagnets, *Phys. Rev. Lett.* **109**, 077201 (2012).
- [58] D. C. Johnston, Magnetic dipole interactions in crystals, *Phys. Rev. B* **93**, 014421 (2016).
- [59] D. C. Johnston, Influence of uniaxial single-ion anisotropy on the magnetic and thermal properties of Heisenberg antiferromagnets within unified molecular field theory, *Phys. Rev. B* **95**, 094421 (2017).
- [60] D. C. Johnston, Influence of classical anisotropy fields on the properties of Heisenberg antiferromagnets within unified molecular field theory, *Phys. Rev. B* **96**, 224428 (2017).
- [61] C. Kittel, *Introduction to Solid State Physics* (Wiley, Hoboken, NJ, 2005).
- [62] P. W. Selwood, *Magnetochemistry*, 2nd Edition (Interscience, New York, 1956), p. 78.
- [63] Metallic Shifts in NMR, Part I, in *Progress in Materials Science*, Vol. 20, edited by B. Chalmers, J. W. Christian, and T. B. Massalski (Pergamon Press, Oxford 1977), Ch. 2.
- [64] A. M. Stewart, Paramagnetic Susceptibilities of Metallic Samarium Compounds, *Phys. Rev. B* **6**, 1985 (1972).
- [65] M. A. Ruderman and C. Kittel, Indirect Exchange Coupling of Nuclear Magnetic Moments by Conduction Electrons, *Phys. Rev.* **96**, 99 (1954).
- [66] T. Kasuya, A Theory of Metallic Ferro- and Antiferromagnetism on Zener's Model, *Prog. Theor. Phys.* **16**, 45 (1956).
- [67] K. Yosida, Magnetic Properties of Cu-Mn Alloys, *Phys. Rev.* **106**, 893 (1957).
- [68] R. J. Goetsch, V. K. Anand, A. Pandey, and D. C. Johnston, Structural, thermal, magnetic, and electronic transport properties of the $\text{LaNi}_2(\text{Ge}_{1-x}\text{P}_x)_2$ system, *Phys. Rev. B* **85**, 054517 (2012).
- [69] H. Wiesmann, M. Gurrvitch, H. Lutz, A. K. Ghosh, B. Schwarz, M. Strongin, P. B. Allen, and J. W. Halley, Simple Model for Characterizing the Electrical Resistivity in A-15 Superconductors, *Phys. Rev. Lett.* **38**, 782 (1977).
- [70] B. Chakraborty and P. B. Allen, Boltzmann Theory Generalized to Include Band Mixing: A Possible Theory for "Resistivity Saturation" in Metals, *Phys. Rev. Lett.* **42**, 736 (1979).
- [71] N. F. Mott and H. Jones, *The Theory of the Properties of Metals and Alloys* (Clarendon press, Oxford, 1936).
- [72] N. F. Mott, The Resistance and Thermoelectric Properties of the Transition Metals, *Proc. Royal Soc.* **156**, 368, 1936.
- [73] N. F. Mott, The Electrical Conductivity of Transition Metals, *Proc. Royal Soc. Lond. A* **153**, 699, 1936.
- [74] A. B. Pippard, *Magnetoresistance in Metals*, (Cambridge University Press, Cambridge, 1989)
- [75] B. Delley, From molecules to solids with the DMol³ approach, *J. Chem. Phys.* **113**, 7756 (2000).
- [76] J. P. Perdew, K. Burke, and M. Ernzerhof, Generalized Gradient Approximation Made Simple, *Phys. Rev. Lett.* **77**, 3865 (1996).
- [77] P. E. Blöchl, O. Jepsen, and O. K. Andersen, Improved tetrahedron method for Brillouin-zone integrations, *Phys. Rev. B* **49**, 16 223 (1994).
- [78] T. Nagamiya, Helical Spin Ordering—1 Theory of Helical Spin Configurations, in *Solid State Physics*, Vol. 20, edited by F. Seitz, D. Turnbull, and H. Ehrenreich (Academic Press, New York, 1967), pp. 305–411.
- [79] Y. Xiao, Y. Su, M. Meven, R. Mittal, C. M. N. Kumar, T. Chatterji, S. Price, J. Persson, N. Kumar, S. K. Dhar, A. Thamizhavel, and Th. Brueckel, Magnetic structure of EuFe_2As_2 determined by single-crystal neutron diffraction, *Phys. Rev. B* **80**, 174424 (2009).
- [80] S. Das, K. McFadden, Y. Singh, R. Nath, A. Ellern, and D. C. Johnston, Structural, magnetic, thermal, and electronic transport properties of single-crystal EuPd_2Sb_2 , *Phys. Rev. B* **81**, 054425 (2010).
- [81] V. K. Anand and D. C. Johnston, Antiferromagnetism in EuCu_2As_2 and $\text{EuCu}_{1.82}\text{Sb}_2$ single crystals, *Phys. Rev. B* **91**, 184403 (2015).
- [82] D. H. Ryan, J. M. Cadogan, V. K. Anand, D. C. Johnston, and R. Flacau, The magnetic structure of EuCu_2Sb_2 , *J. Phys.: Condens. Matter* **27**, 206002 (2015).
- [83] H. E. Nigh, S. Legvold, and F. H. Spedding, Magnetization and Electrical Resistivity of Gadolinium Single Crystals, *Phys. Rev.* **132**, 1092 (1963).
- [84] B. N. Harmon and A. J. Freeman, Spin-polarized energy-band structure, conduction-electron polarization, spin densities, and the neutron magnetic form factor of ferromagnetic gadolinium, *Phys. Rev. B* **10**, 1979 (1974).